



**HAL**  
open science

## Plastic and fracture behavior of a dual phase steel sheet under quasi-static and dynamic loadings

Valentin Davaze, Nicolas Vallino, Sylvia Feld-Payet, Bertrand Langrand,  
Jacques Besson

► **To cite this version:**

Valentin Davaze, Nicolas Vallino, Sylvia Feld-Payet, Bertrand Langrand, Jacques Besson. Plastic and fracture behavior of a dual phase steel sheet under quasi-static and dynamic loadings. *Engineering Fracture Mechanics*, 2020, 235, pp.107165. 10.1016/j.engfracmech.2020.107165 . hal-03167467

**HAL Id: hal-03167467**

**<https://hal.science/hal-03167467>**

Submitted on 12 Mar 2021

**HAL** is a multi-disciplinary open access archive for the deposit and dissemination of scientific research documents, whether they are published or not. The documents may come from teaching and research institutions in France or abroad, or from public or private research centers.

L'archive ouverte pluridisciplinaire **HAL**, est destinée au dépôt et à la diffusion de documents scientifiques de niveau recherche, publiés ou non, émanant des établissements d'enseignement et de recherche français ou étrangers, des laboratoires publics ou privés.

# Plastic and fracture behavior of a dual phase steel sheet under quasi-static and dynamic loadings.

Valentin Davaze<sup>a</sup>, Nicolas Vallino<sup>a</sup>, Sylvia Feld-Payet<sup>b</sup>, Bertrand Langrand<sup>c</sup>, Jacques Besson<sup>d</sup>

<sup>a</sup>Groupe PSA, Technical Center of Vélizy, F-78140 Vélizy-Villacoublay, France

<sup>b</sup>DMAS, ONERA, Université Paris Saclay, F-92322 Châtillon - France

<sup>c</sup>DMAS, ONERA, F-59014 Lille - France

<sup>d</sup>Centre des Matériaux, Mines ParisTech, CNRS UMR 7633, PSL Research-University, Paris, France

---

## Abstract

Crack prediction is an important step of car design: its accuracy is crucial to avoid additional development costs and delays. The prediction of steel or aluminium sheets tearing is particularly challenging, and its simulation is not always reliable yet. This could be explained by the use of too simple fracture criteria based on a critical plastic strain that are uncoupled with the constitutive behavior (*i.e.* the material response is not affected by damage). To overcome this problem, coupled damage models are proposed in the literature. To select the appropriate constitutive equations to model the plastic and fracture behavior of a given material, various characterization tests are needed. A comprehensive experimental campaign that covers a wide range of stress states and loading rates was conducted. All tests can be performed on a tensile machine. From the results, an original set of constitutive equations was chosen from the literature to propose an extended Gurson-based damage model. A practical parameter identification procedure is proposed to calibrate the model on a few relevant specimen geometries. The model is then validated on another set of specimen geometries: comparisons between test results and simulations show a good agreement in terms of load-displacement curves for both quasi-static and dynamic loading conditions.

**Keywords:** Dual-phase steel, dynamic behavior, ductile fracture, damage model, crash

---

## Nomenclature

DP Dual-phase

$\eta$  Stress triaxiality

$\theta$  Lode angle

L T D Anisotropy directions

YS Yield stress

UTS Ultimate tensile strength

R Radius

W Width

NT Notched

FN Flat Notched

CCP Center Crack Panel

EDM Electro-Discharge Machining

HST High Speed Tensile

DIC Digital Image Correlation

SEM Scanning Electron Microscope

$\dot{u}$  Loading rate

$E$  Young modulus

$\nu$  Poisson ratio

$R(p)$  Hardening law

$R_e$  Initial yield stress

$H$	Linear hardening	$\dot{\epsilon}_{is}, \dot{\epsilon}_{ad}$	Isothermal/adiabatic plastic strain rate
$Q, b$	Parameters of Voce [1] hardening	$f_n, f_g, f_{sh}$	Nucleation, growth, shear void volume fraction
$f$	Plastic yield function	$\mathcal{H}(\cdot)$	Heaviside function
$\sigma_1, \sigma_2, \sigma_3$	Three principal stresses	$\epsilon_d$	Nucleation trigger plastic strain
$\sigma_F$	Flow stress	$A$	Nucleation slope
$\bar{\sigma}$	Equivalent stress	$\text{Tr}(\cdot)$	Trace of a tensor
$c$	Drucker [2] criterion parameter	$k_w$	Nahshon and Hutchinson [7] parameter
$J_2$	Second deviatoric invariant	$w$	Nahshon and Hutchinson [7] weight function
$J_3$	Third deviatoric invariant	$\theta$	Lode angle
$\bar{\sigma}, \bar{s}$	Cauchy and deviatoric stress tensor	$f_t, f^*$	Total and effective void volume fraction
$\det(\cdot)$	Determinant of a tensor	$f_c, f_r$	Critical and rupture void volume fraction
$\dot{\epsilon}_0$	Inviscid limit plastic strain rate	GTN	Gurson-Tvergaard-Needleman[8, 9, 10]
$C$	Johnson-Cook [3] parameter	$\phi$	GTN plastic yield criterion
$\mu$	Zhao [4] thermal softening parameter	$q_1, q_2$	GTN criterion parameters
$\eta_k$	Taylor-Quinney [5] coefficient	$L_e$	Mesh size
$\rho$	Material density	NICE	Next Increment Correct Error numerical scheme [11]
$C_p$	Heat capacity		
$\dot{\bar{\epsilon}}_p$	Plastic strain rate tensor		
$\omega$	Roth and Mohr [6] weight function		

## 1. Introduction

In the automotive industry, the ecological concern leads to making car bodies from thin metallic (steel or aluminium) sheets. This helps reducing car weight and increases fuel efficiency. However, these very thin structures can be subjected to tearing, especially in crash conditions. As tearing should be avoided, simulations are carried out to ensure structural integrity. However, ductile failure initiation and crack tearing are not yet reliably predicted by simulations. And, when a crack is detected by certification tests, parts and tools have to be re-designed, which increases the development cost and entails delays.

The poor numerical prediction of cracking can be explained by the use of too simple solutions such as basic fracture criteria used to 'delete' elements from the simulation when a critical value of plastic strain is reached. Although these fracture criteria are easy to implement, and often require a limited number of parameters to be identified, they do not always take into account the effect of stress triaxiality (here referred to as  $\eta$ ) and the Lode angle ( $\theta$ ) which are known to control crack initiation. To improve the prediction of fracture criteria for crash simulations purposes, commonly used solutions are Rice and Tracey [12] (micromechanically based) or Johnson–Cook [13] (phenomenologically based) criteria which both consider a decrease of the plastic strain at failure as stress triaxiality increases. This assumption, mostly verified at high stress triaxiality ( $\eta > 1/3$ ), is not always correct for a wide range of stress triaxialities. Indeed, a potential drop of fracture strain can be also observed at very low stress triaxiality ( $\eta < 1/3$ ), under shear conditions for instance. In order to remedy this shortcoming, Bai and Wierzbicki [14] have proposed a

ductile failure criterion known as the Modified Mohr–Coulomb [15, 16] (MMC) criterion, which is usually used to describe the failure of brittle materials. This MMC criterion can predict the strain at failure for a wide range of stress triaxiality and Lode angle combinations. The MMC criterion was further extended in [17] using the Hershey [18]/Hosford [19] equivalent stress instead of the Tresca stress [20]. According to the authors, a better prediction under plane stress conditions is obtained. The Hosford-Coulomb failure criterion was also improved to introduce the effect of other phenomena such as strain-rate dependency [6] or more recently necking effect [21, 22] for shell element applications. However, any improvement of these criteria leads to an increase of the number of parameters to identify and requires complex testing procedures to measure the plastic strain at failure for various stress triaxialities and Lode angle values. Moreover, using fracture criteria, damage does not influence the elasto-plastic behavior. This means that stress softening is not represented, which can cause a poor description of strain localization and of the crack path as the material does not lose its load-carrying capacity. From the numerical point of view, another difficulty may arise when performing simulations for dynamic problems (*e.g.* crash): when a critical value is reached for a given number of integration points in an element, this “sound” (*i.e.* undamaged) element is removed from the computation. This causes a sudden drop of the stresses at the material point that can lead to dynamic instabilities.

To improve the numerical prediction of ductile fracture in crash simulations, some contributions [23, 24, 25] have considered, instead of fracture criteria, the use of coupled damage models, especially micromechanically based Gurson type models. These models consist in computing a damage variable generating stress softening and possibly offering a better representation of strain localisation and the crack path. Numerically, if element deletion is then applied to fully broken elements it does not create spurious elastic waves in dynamic computations. Many damage models (see *e.g.* review in [26, 27]) are designed to take into account the effect of stress triaxiality and/or Lode angle so as to be able to distinguish shear cracks at low triaxiality and necking cracks at high triaxiality.

This paper proposes to evaluate the ability of coupled damage models to predict fracture for a wide range of stress states on a representative ductile material commonly used in automotive industry as a shock absorber in crash: a DP450 “*dual-phase*” steel sheet. In order to build, calibrate and validate a model, a comprehensive experimental study, described in section 2, is carried out on various test specimens which can be easily tested on a tensile test machine. Several geometries are tested so as to vary stress states. Since crash simulations require the constitutive model to be able to predict failure at both very low and high velocities, the tests are performed at both low and high loading rates. The effect of temperature on the material behavior is also studied. On the basis of the observed phenomena, a plasticity model containing hardening, viscosity and self-heating is first proposed in section 4. The damage effects are represented using a modified version of the Gurson-Tvergaard-Needleman [10] model which is introduced in section 5. The strategy used to determine the model parameters is detailed in section 6. Finally, the numerical validation of this original constitutive model is done by comparing tests on specimens that have not been used to identify the model parameters and the corresponding simulations in the section 7. The originality of this work lies in the combination of a large experimental database, including specimens allowing for stable crack growth, with the proposed constitutive model for a wide range of loading rates and its verification.

## 2. Material and experimental procedure

In this first section, a brief description of the studied DP450 steel is given, and the experimental campaign is detailed.

### 2.1. DP450 “dual-phase” Steel

The material of this study is a dual-phase DP450 steel which is representative of the type of steel used for sheets in the car industry. Its large maximum elongation and its low yield stress are good properties for metal forming process and shock absorption in crash conditions. This DP steel is composed of a small amount of martensite within a ferrite matrix (see [fig. 1](#)). Alloying elements are given in [tab. 1](#). The material is supplied as a 1.18 mm thick sheet obtained by rolling process. In the following the rolling direction will be referred to as L (0°), the transverse direction as T (90°) and the diagonal direction as D (45°).

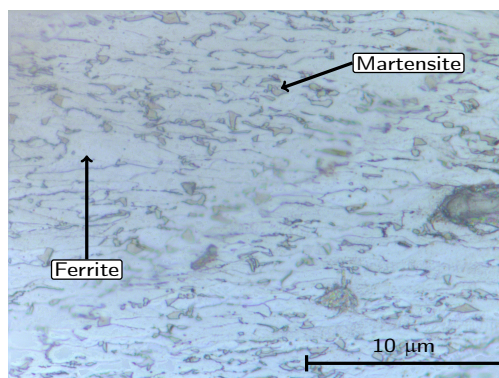


**Figure 1:** Microstructure of DP450 steel after nital etching.

C	Mn	Si	P	S	Cu	Al	Fe
0.08	1.6	0.4	< 0.05	< 0.01	< 0.2	< 1.	bal.

**Table 1:** Nominal chemical composition (weight %)

### 2.2. Experimental procedures

A comprehensive experimental campaign was performed to highlight all possible phenomena that may have an influence on crack initiation and propagation. Almost 120 tests were carried out on specimens with 9 different geometries to vary stress state (see [fig. 2](#)). All the specimen geometries can be tested on a tensile machine. These specimens were tested at different loading rates and temperatures. Flat standard (see [fig. 2a](#)) and large (see [fig. 2b](#)) specimens were used to characterize the plastic behavior of the material. Strain rates were selected so that they correspond to rates in highly deformed zones during crash *i.e.* up to  $200 \text{ s}^{-1}$ .

Notched specimens, referred to as NT1 ([fig. 2c](#)), NT2 ([fig. 2d](#)), V45 ([fig. 2e](#)), Central hole ([fig. 2f](#)) and FN ([fig. 2i](#)), are relevant to analyze the effect of high stress triaxiality on plasticity and crack initiation. The smaller the notch is, the higher the stress triaxiality. To study crack initiation at lower stress triaxiality, a shear “M-shape” specimen ([fig. 2g](#)) was also used. Finally, crack propagation was studied using a Center Crack Panel (CCP) specimen ([fig. 2h](#)). A very thin notch was introduced in this specimen using Electro-Discharge Machining (EDM); the notch radius is, in that case, 0.1 mm. Note that because of the steel sheet small thickness (1.18 mm), buckling cannot be avoided in compression tests so that negative stress triaxiality was not considered in this experimental study.

Some of these specimens (std. flat, NT1, V45, M-shape and CCP) were tested at low and high velocities using two different testing machines. For high velocities, the geometries of specimens tested employing the

FastGrip system (see fig. 3c) needed to be modified so as to increase their lengths. The width of M-shape and CCP specimens was also reduced. This last modification has no influence in the case of the M-shape specimen as the strained area remains unchanged. It is however necessary to distinguish between the CCP specimens (CCP and CCP-dyna) as the initial ligament is reduced for specimens tested at high rates. The specific dimensions used at high rates are outlined in red in fig. 2. In all cases, it was checked that the prescribed velocity is such that the strain rates reached locally for the notched specimens are within the experimental range prescribed for the flat tensile specimens.

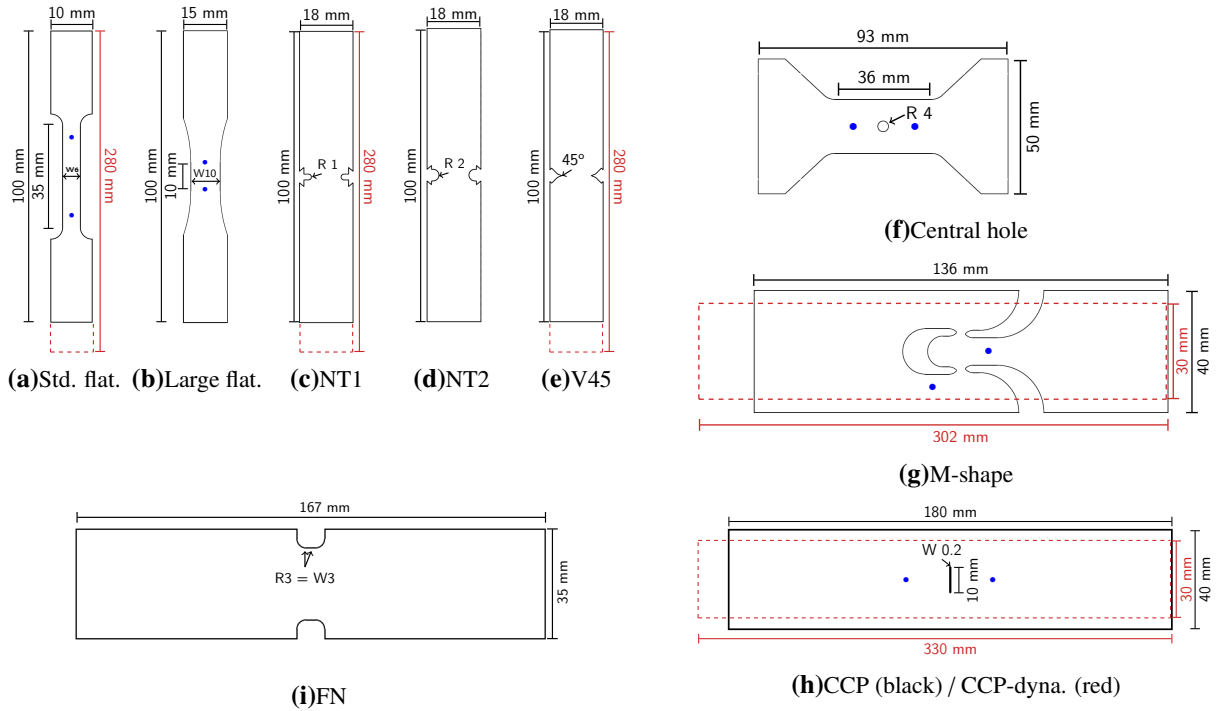


**Figure 2:** Specimens used in the experimental campaign (measurement points are marked with •). Specific dimensions used at high rates are outlined in red.

Experiments were conducted on tensile hydraulic machines: MTS 100 kN and MTS 810 Mat. system (see fig. 3a) for the quasi-static tests, Schenck actuator (see fig. 3b) and HST Instron VHS 65/80 with FastGrip system (see fig. 3c) for the dynamic tests. Measurements are taken using MTS extensometers: longitudinal 632.11 (gage length = 27 mm) for relative displacement on standard flat, and Central Hole specimens and clips (632.02) for notch opening on NT1, NT2 and V45 specimens. Shadow tracking [28] (see fig. 4) was also used to assess the transverse strain on the same specimens. The relative precision of the measure is about  $2\delta/l_0$  with  $\delta = 1$  to 2 pixels.  $l_0$  is the length being tracked (see fig. 4). The experiments were carried out so that  $l_0 \approx 1000$  pixels. Consequently the accuracy on the transverse deformation is 2 to 4%. To reduce noise, results were consequently filtered. In the case of some flat tensile specimens, the axial extensometer was removed during the test so as to be able to monitor transverse strains beyond necking. At high loading rates, Fiedler doppler lasers replaced longitudinal extensometers for standard flat specimens. For Large flat, NT1, V45, M-shape and CCP/CCP-dyna geometries, relative displacement was measured by Digital Image Correlation (DIC) with virtual extensometers. Measurement points for some

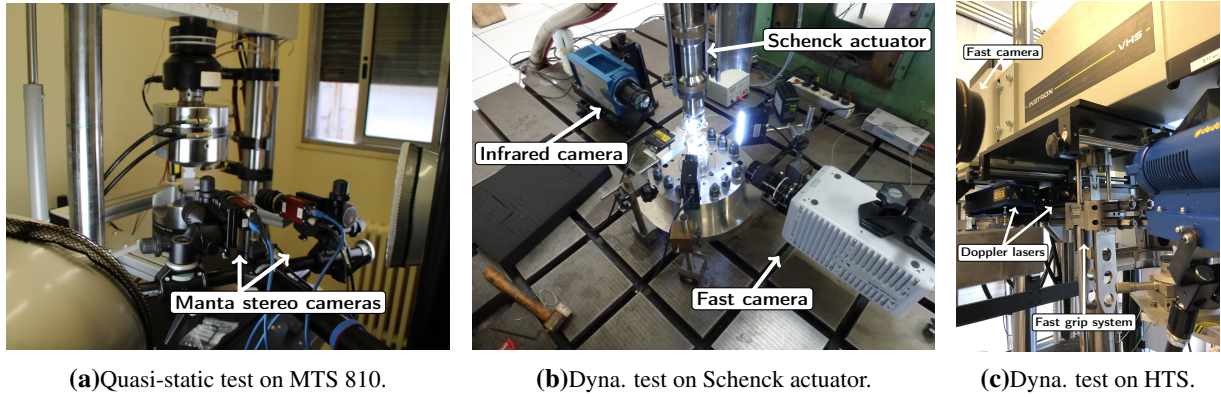


**Figure 3:** Experimental setups and measure devices for quasi-static and dynamic tensile tests.

geometries are marked with • on fig. 2. Cameras are Diagnostic Instrument Monochrome 14.1 for shadow tracking, Manta Allied Vision and Photron FastCam respectively for quasi-static and dynamic tests. An infrared camera (see fig. 3b) was also used to evidence possible self-heating in the case of dynamic tests. All tests were repeated two or three times to check reproducibility, which was found to be very good.

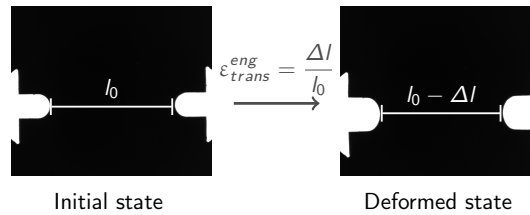


**Figure 4:** Illustration of shadow tracking measure on NT1 specimen.

### 3. Main experimental results

For the sake of clarity and brevity, a selection of experimental results among the tests listed in tab. 2 is presented here to outline the main observed phenomena. This section is organized as follows. First the elasto-plastic behavior under quasi-static loading is described. Strain rate dependence and related adiabatic heating are then presented. Finally damage growth and crack propagation are detailed.

#### 3.1. Elasto-plastic behavior

Tensile tests on standard flat specimens (see fig. 2a) were carried out along several directions in the sheet plane from L ( $0^\circ$ ) to T ( $90^\circ$ ), by steps of  $15^\circ$ , to evaluate material anisotropy. These tests were performed at low strain rate ( $0.001 \text{ s}^{-1}$ ) and room temperature ( $20^\circ\text{C}$ ). Measures of longitudinal and transverse strains allow to evaluate the Lankford coefficient for all directions.

The true stress—strain curves for directions L, D and T are given in fig. 5a. Direction T appears slightly less resistant than directions L and D. The average yield stress is equal to 283 MPa and the Ultimate Tensile Stress is 490 MPa. The evolution of the transverse strain is plotted as a function of the longitudinal strain in fig. 5b, evidencing a slight anisotropy.

The in-plane variations of yield stress (see fig. 5c), ultimate tensile strength (see fig. 5d) and Lankford coefficient (see fig. 5e), allow to obtain a more precise characterization of the material anisotropy. Anisotropy is very limited for stresses and slightly more pronounced in the case of the Lankford coefficient. In the following the material will be considered as isotropic for the sake of simplicity. Note that in practice, forming of parts in automotive industry is conducted without considering sheet orientation. Nevertheless, all remaining quasi-static tests were performed along both L and T directions to check for possible anisotropic ductility which appeared in fact to be very limited. For that reason, tests for a given specimen and different loading directions were averaged. Consequently experimental scatter will also integrate the effect of anisotropy. For dynamic loading, the orientation of specimens was no longer considered so as to reduce the number of repeated tests.

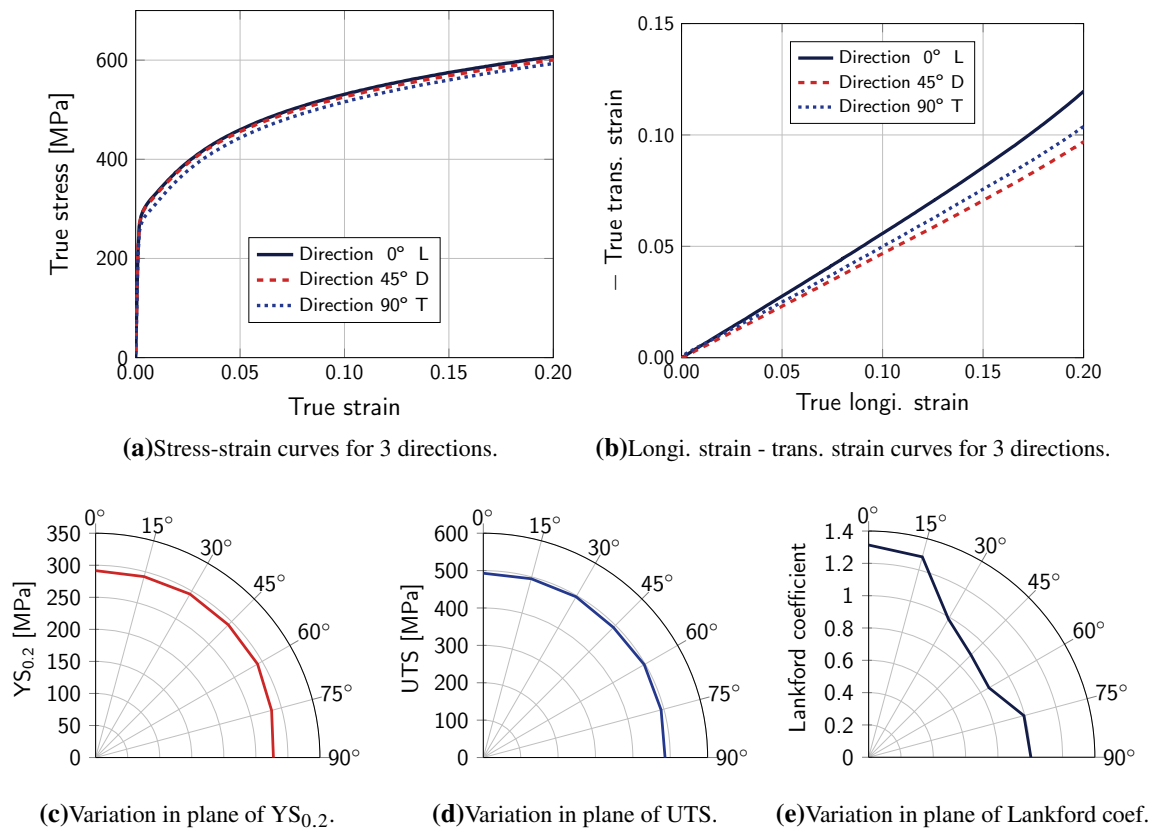


**Figure 5:** Results obtained with quasi-static tensile test on standard flat specimen ( $\dot{\epsilon} = 0.001 \text{ s}^{-1}$ ) along several directions in the plane to evaluate anisotropy.

### 3.2. Strain-rate and temperature effects

As a car crash is a dynamic event, it is necessary to characterize the effect of loading rate on the behavior of the material. To do so, dynamic tensile tests were performed on several geometries. Load-displacement curves obtained on FN specimens are given in fig. 6a (note that the for the highest velocity of  $1.0 \text{ m.s}^{-1}$ , results were filtered which made the elastic response disappear from the curve). A significant gain in strength with increasing loading rate is noticed which shows that the material is strain-rate dependent.

The displacement at failure decreases with a steeper load drop. Infrared pictures showed a significant temperature increase after the onset of necking and during cracking as exemplified in fig. 6b. In that case, an increase of 100°C with respect to room temperature is observed just before failure for an intermediate (*i.e.* without inertia effects, no oscillations on the load) loading rate equal to  $\dot{u} = 8.33 \text{ mm.s}^{-1}$ . This corresponds to quasi-adiabatic heating. Note that temperature increase in tensile bars at necking is moderate (about 25°C). The local increase in temperature in the notched area during necking and failure is believed to be responsible for the loss of macroscopic ductility (defined here as the displacement at full failure). This trend is not evidenced in other studies on various DP steels (higher grades than in this study). For instance, [29] (DP800) found that loading rate has a very moderate effect on ductility. The same authors reported a similar trend on a DP590 material [6]. It is found in [30] (DP780) that ductility (measured as the reduction in area) increases with increasing loading rate.

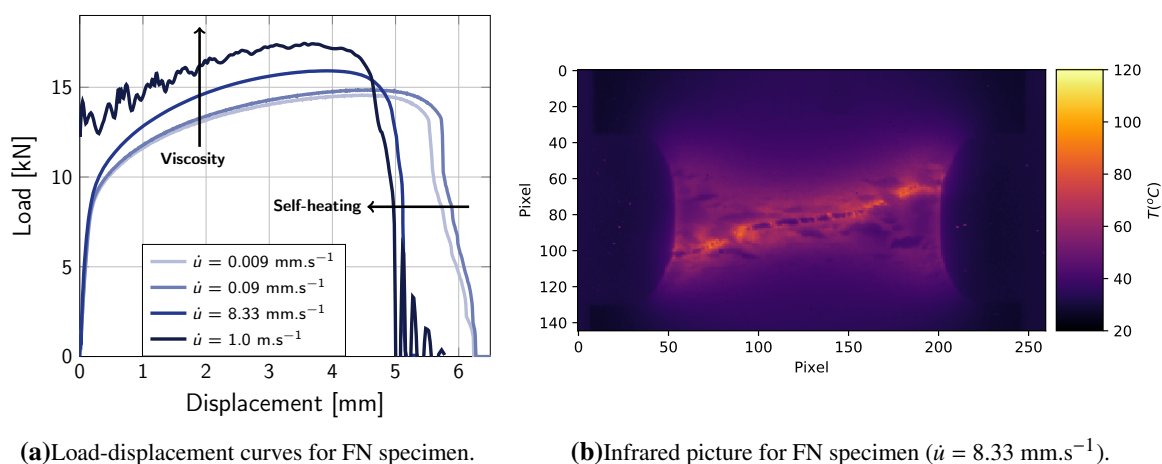
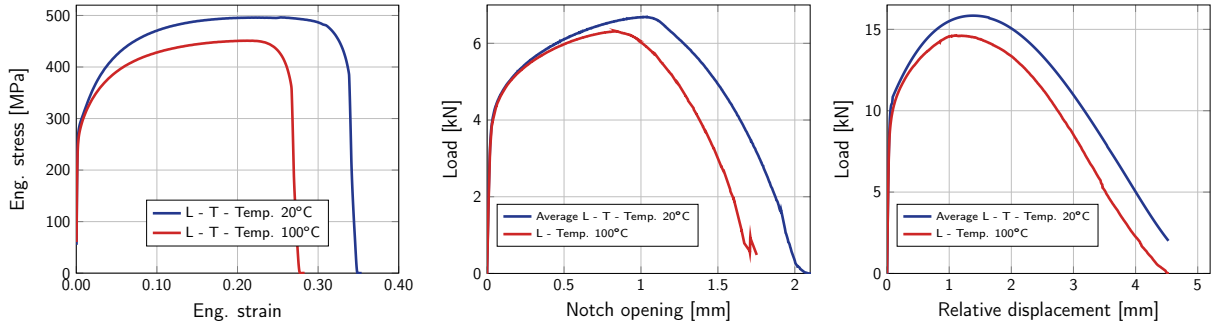


**Figure 6:** Results obtained on FN specimen at several loading rates.

In order to develop constitutive equations, it is therefore necessary to characterize the effect of the temperature alone on the material behavior. For that purpose quasi-static tensile tests were carried out at 100°C. The low loading rate ensures to keep the isothermal conditions as self-heating only appears at high rates. Several specimens were tested: standard flat, V45, and CCP. An oven and thermocouples were used to regulate the temperature of the specimens. Results obtained on these specimens are presented in fig. 7. A significant loss of strength is observed with increasing specimen temperature. A similar trend was found in [29] on a DP800 steel. In this last study it was also shown that strength and ductility increase for temperatures between 180 and 300°C. The model developed below will only account for the temperature effects on hardening and not on damage. The effect on failure will not be accounted for as most of the deformation/damage occurs well below 100°C.

### 3.3. Crack initiation and propagation

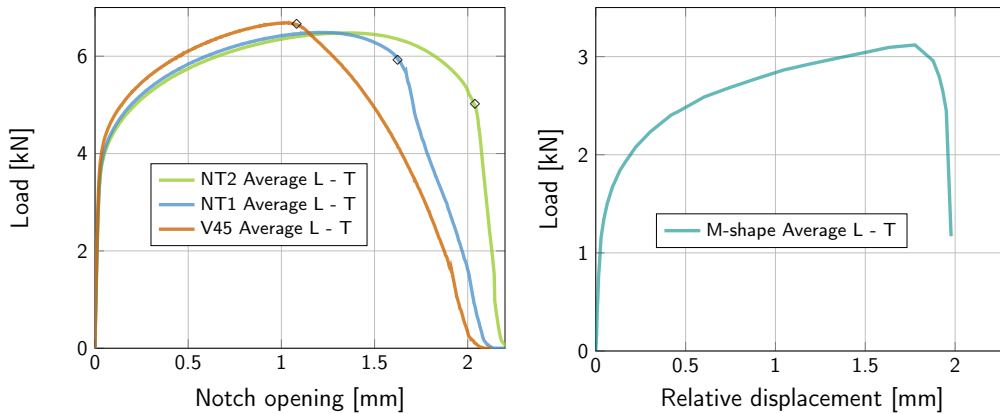
Quasi-static tensile tests were performed on notched and shear specimens along T and L directions. Averaged results for several specimens are given in fig. 8. NT2, NT1 and V45 specimens (fig. 8a) have the same minimum cross section and allow positioning the clip extensometer at the same location. These notched specimens have a relatively high stress triaxiality before crack initiation ( $\eta > 0.35$ ). The highest value is reached in the case of the V45 specimen so that it exhibits higher load levels before crack initiation



(a) Stress-strain curves at different temperatures for standard flat specimen. (b) V45 results at different temperatures. (c) CCP results at different temperatures.

**Figure 7:** Effects of sole temperature on the material behavior.

which was manually detected based on the photographs taken during the tests (marked by  $\diamond$  in fig. 8a). However, as the sheet is relatively thin triaxiality levels remain limited so that the maximum load levels of all specimens are close. The notch opening at crack initiation decreases with notch severity illustrating the usual dependence of ductility on stress triaxiality. Crack propagation is stable (*i.e.* no sudden load drop) in all cases up to complete failure. Load decrease is very steep for NT2 specimens but gradual for V45, which allows to use this specimen to characterize crack propagation. The M-shape specimen (see fig. 8b) shows an abrupt load decrease which limits its use to only characterizes initiation. This specimen (see fig. 2g) has two ligaments so that one of them fails first which causes dissymmetric failure. The test is then stopped after this first failure which explains that the final recorded load is not equal to 0.



(a) Notched specimens ( $\dot{u} = 0.002 \text{ mm.s}^{-1}$ ).

(b) Shear specimen ( $\dot{u} = 0.003 \text{ mm.s}^{-1}$ ).

**Figure 8:** Results obtained with quasi-static tests on notched and shear specimens.

For a better understanding of damage growth leading to failure, fracture surfaces were observed using a Scanning Electron Microscope (SEM). Fig. 9 shows a typical ductile fracture surface obtained for a NT1 specimen. Numerous small dimples can be observed. A polished longitudinal cross section is also shown in fig. 9b. Voids are exhibited below the fracture surface up to a distance of about  $500 \mu\text{m}$ . It was checked

that outside the necked area damage was not initiated. Failure thus appears to be caused by void nucleation and growth in the material. Polished cross sections of the unstrained material showed no initial damage.

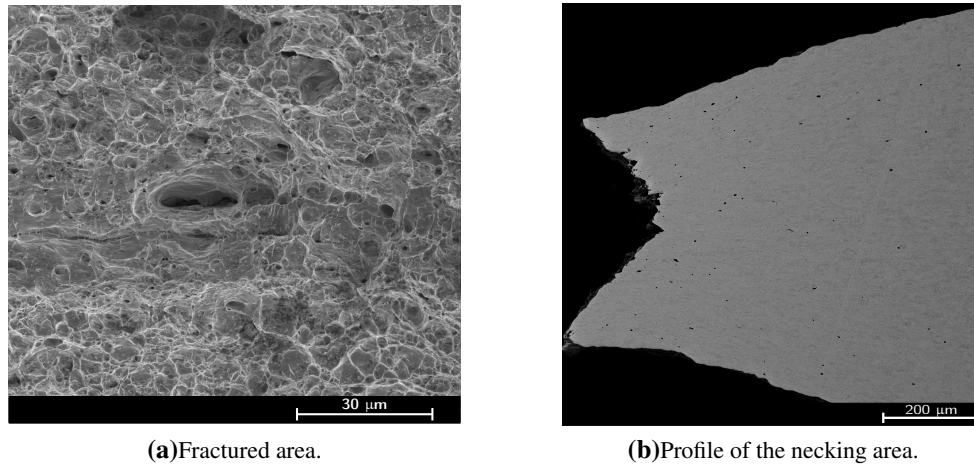


**Figure 9:** Scanning Electron Microscope pictures of a fractured NT1 specimen.

### 3.4. Summary

The summary table of the performed tests for all specimens, loading rates and temperatures is given in [tab. 2](#). From the observations made thanks to these tests, it is possible to summarize the phenomena that have an influence on plasticity, crack initiation and propagation:

1. Plasticity : isotropic with hardening,
2. Strain rate sensitivity : increase in strength with the increasing strain rate,
3. Self-heating : heat generation at high strain rate that leads to a loss of macroscopic ductility,
4. Damage : nucleation, growth and coalescence of cavities responsible for fracture.

The next two sections of this study introduce the constitutive equations chosen from the literature to represent all these phenomena in a constitutive model. Constitutive equations for plasticity describing hardening, viscosity and self-heating are first introduced in [section 4](#). These constitutive equations are then extended to account for damage in [section 5](#). The identification strategy is detailed in [section 6](#).

## 4. Constitutive equations for plasticity

The constitutive equations for plasticity are first described in this section. The hardening law, the plasticity yield criterion, the rate-dependency model and the rule for quasi adiabatic self-heating effects are detailed. Note that the elastic behavior is supposed to be linear and isotropic. The Young modulus is  $E = 192$  GPa and obtained from experimental results in directions L and T. The Poisson ratio  $\nu = 0.3$  is chosen from [\[31\]](#).

	0.002 mm.s <sup>-1</sup>	0.003 mm.s <sup>-1</sup>	0.004 mm.s <sup>-1</sup>	0.009 mm.s <sup>-1</sup>	0.035 mm.s <sup>-1</sup>
Standard flat	-	-	-	-	2 L 2 T ●★
Large flat	-	-	-	-	-
NT1	2 L 2 T ★★	-	-	-	-
NT2	2 L 2 T ★	-	-	-	-
V45	2 L 2 T ●★	-	-	-	-
Central hole	-	-	2 L 2 T	-	-
M-shape	-	2 L 2 T ★★	-	-	-
CCP	-	-	2 L 2 T ●	-	-
FN	-	-	-	2 L	-
	0.04 mm.s <sup>-1</sup>	0.0833 mm.s <sup>-1</sup>	0.09 mm.s <sup>-1</sup>	8.33 mm.s <sup>-1</sup>	0.2 m.s <sup>-1</sup>
Standard flat	2 L ★	-	-	-	-
Large flat	-	3 ★	-	3 ★	-
NT1	-	-	-	-	2
NT2	-	-	-	-	-
V45	-	-	-	-	2
Central hole	-	-	-	-	-
M-shape	-	-	-	-	-
CCP	-	-	-	-	-
FN	-	2	3	3	-
	0.5 m.s <sup>-1</sup>	1.0 m.s <sup>-1</sup>	3.0 m.s <sup>-1</sup>	5.0 m.s <sup>-1</sup>	7 m.s <sup>-1</sup>
Standard flat	-	2 ★	2 ★	2 ★	2 ★
Large flat	-	3 ★	-	-	-
NT1	2	2	2	-	-
NT2	2	2	2	-	-
V45	2	2	2	-	-
Central hole	-	-	-	-	-
M-shape	2	2	2	-	-
CCP dyna	-	2	2	-	2
FN	-	3	-	-	-

**Table 2:** Table summarizing the number of tests per configuration realized in the experimental campaign at room temperature of 20°C. Tests also performed at 100°C are marked with a red dot ●. Those used for the plasticity constitutive model identification are marked with a yellow star ★, and those used for the damage constitutive model are marked with a blue star ★. Tests realized on standard flat specimens to study anisotropy are not included.

#### 4.1. Hardening model

Work-hardening has been observed on experimental results (see fig. 5a). To model this phenomenon, a Voce type law [1] is often used in the literature [32]. This law leads to a maximum value of the flow stress. However, Le Maout *et al.* [33] have mentioned that for tests realized up to failure, an additional linear term might be considered to represent hardening at high strains. Thus the Voce law is modified accordingly by adding a linear hardening term to obtain the following expression for the flow stress:

$$\sigma_F = R(p) = R_e + Hp + Q(1 - \exp(-bp)) \quad (1)$$

where  $R_e$  is the initial tensile yield stress,  $H$  the linear hardening coefficient,  $p$  the cumulated plastic strain,  $Q$  and  $b$  the two Voce parameters.

#### 4.2. Plastic yield criterion

The choice of a plastic yield criterion requires several tests at different stress triaxialities. Notched specimens (NT1, NT2, V45) and M-shape shear specimens are used to determine and identify the appropriate isotropic plastic yield criterion. Considered candidates are Tresca [20], von Mises [34], Hershey/Hosford [18, 19] and Drucker [2] yield criteria. The best fit is obtained using the Drucker criterion. Although the Hosford model leads to predictions which are quite close, the numerical implementation of the Drucker criterion is easier. The Drucker yield criterion is expressed as:

$$f = \bar{\sigma} - \sigma_F \quad \text{with} \quad \bar{\sigma} = \sqrt[6]{\left(\frac{1}{27} - c\frac{4}{729}\right)^{-1} (J_2^3 - cJ_3^2)} \quad (2)$$

where  $\bar{\sigma}$  is the equivalent stress associated to the Drucker criterion,  $\sigma_F$  the flow stress and  $c$  the Drucker parameter.  $J_2$  and  $J_3$  designate respectively the second and third deviatoric invariants which are expressed as:

$$J_2 = \frac{1}{2} \bar{\bar{s}} : \bar{\bar{s}} \quad J_3 = \det(\bar{\bar{s}}) \quad (3)$$

where  $\bar{\bar{s}}$  is the deviatoric stress tensor and  $\det(\cdot)$  the determinant. If  $c = 0$ , the  $J_2$ —plasticity of von Mises is recovered. Depending on the value of the  $c$  parameter, the Drucker yield surface lies between a smoothed Tresca surface ( $c = 2.25$ ) and the upper bound of Mendelson [35] ( $c = -27/8$ ). Note that the Drucker yield criterion depends on the Lode angle (see below eq. (11)) as it is expressed as a function of both  $J_2$  and  $J_3$ .

#### 4.3. Strain rate dependence

A rate-dependent behavior has also been highlighted with tensile tests at high velocities. To represent this phenomenon, several models taken from the literature can be considered. The Johnson–Cook [3] formula is most the commonly used rate-dependent approach in the automotive industry. Other well known works can be cited as Zerilli–Armstrong [37] or Zhao [4] models. In this paper, it is first chosen to consider the Johnson–Cook approach. The flow stress is consequently modified by a multiplicative factor depending on the strain rate as follows:

$$\sigma_F = R(p) \underbrace{\left(1 + C \left\langle \ln \frac{\dot{p}}{\dot{\epsilon}_0} \right\rangle_+\right)}_{\text{Strain rate dependence}} \quad (4)$$

where  $C > 0$  is a parameter;  $\dot{\epsilon}_0$  is the strain-rate below which strain dependency effects are negligible and  $\langle \cdot \rangle_+$  designates the Macauley brackets. This equation implies that viscous effects appear as soon as the plastic strain rate  $\dot{p}$  is higher than the quasi-static limit strain-rate  $\dot{\epsilon}_0$ .

Regarding the other models mentioned above, the physically based Zerilli–Armstrong model appears to be much more difficult to identify. Zhao rate dependent model is a good candidate in the case where experimental  $\sigma_F - \langle \ln \dot{p} / \dot{\epsilon}_0 \rangle_+$  curves are not linear. This case can be observed at very high strain-rates ( $\dot{\epsilon} > 300 \text{ s}^{-1}$ ). However, using Zhao model implies an increase in the number of parameters to be identified. Similarly, in a recent work, Sarraf *et al.* [32] have proposed a modified version of Johnson–Cook rate dependent model so as to make it "non-linear" by using  $\langle \ln \dot{p} / \dot{\epsilon}_0 \rangle_+^n$  instead of  $\langle \ln \dot{p} / \dot{\epsilon}_0 \rangle_+$  where  $n$  is an additional parameter to be identified.

#### 4.4. Thermal softening and self-heating

At high loading rates and high level of plastic strain ( $p > 15\%$ ), self-heating was experimentally observed leading to a loss of macroscopic ductility and a steeper load drop. This increase of temperature leads to a loss of load carrying capacity (thermal softening). Two candidate models have been considered to represent this phenomenon. On the one hand, the Johnson–Cook [3] approach considers a non-linear softening between room temperature and melting temperature. On the other end, the Zhao [4] thermal softening model considers a linear thermal softening which is, according to the author, sufficient for an automotive application since the temperature increase rarely exceeds a few hundred degrees. For this reason, this last model is preferred for this study. Note that both models only have one parameter to identify. Zhao thermal softening equation is introduced in the flow stress expression as:

$$\sigma_F = R(p) \underbrace{\left( 1 + C \left\langle \ln \frac{\dot{p}}{\dot{\epsilon}_0} \right\rangle_+ \right)}_{\text{Viscosity}} \underbrace{(1 - \mu(T - T_{\text{ref}}))}_{\text{Thermal softening}} \quad (5)$$

Strain-rate effects

where  $\mu$  is the only parameter to identify,  $T$  the current temperature and  $T_{\text{ref}}$  the reference temperature used throughout the identification of  $R(p)$ . In this study,  $T_{\text{ref}}$  corresponds to the room temperature ( $20^\circ\text{C}$ ). Strain rate effects result from the combination of rate dependence and thermal softening.

As coupled thermo—mechanical simulations are avoided in the automotive industry to reduce computation time, the evolution of temperature is given by the following expression proposed by Roth and Mohr [6]:

$$\dot{T} = \omega(\dot{p}) \frac{\eta_k}{\rho C_p} \bar{\sigma} : \dot{\bar{\epsilon}}_p \quad (6)$$

where  $\omega$  is a weight function described in eq. (7),  $\eta_k$  is the Taylor–Quinney [5] coefficient,  $\rho$  the density,  $C_p$  the heat capacity,  $\bar{\sigma}$  the stress tensor and  $\dot{\bar{\epsilon}}_p$  the plastic strain rate tensor. The temperature increase corresponds to the conversion of a given percentage ( $\eta_k$ ) of the plastic work into heat. The weight function  $\omega$  is used to obtain a continuous transition between isothermal conditions at low strain rates with no heat generation and quasi-adiabatic conditions at high strain rates with purely adiabatic heat generation. Its expression is:

$$\omega(\dot{p}) = \begin{cases} 0 & \text{if } \dot{p} < \dot{\epsilon}_{is} \\ \frac{(\dot{p} - \dot{\epsilon}_{is})^2 (3\dot{\epsilon}_{ad} - 2\dot{p} - \dot{\epsilon}_{is})}{(\dot{\epsilon}_{ad} - \dot{\epsilon}_{is})^3} & \text{if } \dot{\epsilon}_{is} \leq \dot{p} \leq \dot{\epsilon}_{ad} \\ 1 & \text{if } \dot{p} > \dot{\epsilon}_{ad} \end{cases} \quad (7)$$

where  $\dot{\varepsilon}_{is}$  is the isothermal limit strain rate and  $\dot{\varepsilon}_{ad}$  is the adiabatic limit strain rate. This weight function allows the constitutive model to be used for low loading rates and high loading rates as well. Note that the identification of  $\dot{\varepsilon}_{is}$  and  $\dot{\varepsilon}_{ad}$  is only possible once the damage model is already introduced and identified because adiabatic heating is only very active in areas where damage is high.

## 5. Constitutive equations for damage

The constitutive model is completed by introducing damage effects. In the experimental study, it has been observed that failure of DP450 steel is due to the nucleation and growth of cavities. To represent these phenomena, a modified version of Gurson-Tvergaard-Needleman (GTN) coupled damage model [8, 9, 10] is used. This model considers spherical cavities surrounded by a material matrix in an representative elementary volume. The damage variable  $f_t$  corresponds to the void volume fraction. The GTN model allows representing different damage phenomena: nucleation, growth and coalescence of cavities. In this study, it is assumed that the as-received material is damage free ( $f_t = 0$ ). Voids must thus be first created by nucleation of cavities during plastic deformation. The nucleated void volume fraction (assumed to correspond to martensite/ferrite debonding) is represented by the variable  $f_n$ . Assuming strain controlled nucleation, the nucleation rate is expressed as:  $\dot{f}_n = A_n(\dots)\dot{p}$ . The Gaussian function proposed by Chu and Needleman [38] is often used for  $A_n$ . In this study, the nucleation rate proposed in [31] is used limiting the number of parameters to identify (2 instead of 3). The nucleation rate is then expressed as:

$$\dot{f}_n = \mathcal{H}(p - \varepsilon_d)A\dot{p} \quad (8)$$

where  $\mathcal{H}(\cdot)$  is the Heaviside function and  $\varepsilon_d$  represents the plastic strain for which nucleation starts. The nucleation rate is then considered as constant (parameter  $A$ ). Growth of nucleated voids is represented by the variable  $f_g$ . Its evolution is related to the plastic volume variation as:

$$\dot{f}_g = (1 - f_t)\text{Tr}(\dot{\bar{\varepsilon}}_p) \quad (9)$$

where  $f_t$  is the total void volume fraction (see eq. (12)) and  $\text{Tr}(\cdot)$  is the trace. It can be noticed that the evolution of  $f_g$  strongly depends on stress triaxiality. This means that the higher the triaxiality, the less ductile the material. However, under shear loading, the trace of the plastic strain tensor is null. In that case,  $f_g$  has no effect and fracture of DP450 might not be well predicted. This is a well known issue encountered with the use of classical GTN model. To overcome this difficulty, it is proposed to use the modification introduced by Nahshon and Hutchinson [7]. It considers a third void volume fraction linked to ‘‘shear’’ damage:

$$\dot{f}_{sh} = k_w f_t \underbrace{\left[1 - (\cos(3\theta))^2\right]}_{w(\theta)} \frac{\bar{\bar{s}} : \dot{\bar{\varepsilon}}_p}{\bar{\sigma}} \quad (10)$$

where  $k_w$  is a constant to identify,  $\theta$  is the Lode angle,  $\bar{\bar{s}}$  the deviatoric stress tensor and  $\bar{\sigma}$  the equivalent stress defined by the plastic yield criterion (Drucker in the present case). The Lode angle is expressed as:

$$\cos(3\theta) = \frac{3\sqrt{3}J_3}{2J_2\sqrt{J_2}} \quad (11)$$

The weight function  $w(\theta)$  is such that shear damage is maximum for  $\theta = \pi/6$  (i.e. under shear or plane strain conditions) and equal to zero when  $\theta$  is close to 0 and  $\pi/3$  (any axisymmetric loading conditions).

This implies that shear damage can be activated at high triaxialities under plane strain conditions. To avoid such a behavior, Nielsen and Tveergard [39] have proposed to modify the expression of  $w$  so that it is equal to zero above a given value of the triaxiality. Note that the triaxiality levels considered in [39] correspond to the levels observed in this work. In this paper, it is chosen to keep the original expression given in eq. (10) as a good fit was obtained with the original model only. Other proposals can be found in the literature to improve the GTN model at low stress triaxialities. Pickett *et al.* [23] suggest to add a nucleation mechanism controlled by the shear components of the plastic strain tensor. More recently Malcher *et al.* [40] and Jiang *et al.* [41] have used the GTN model in which the matrix flow stress ( $\sigma_F$ ) is affected by shear damage following the Lemaitre approach [42].

The total void volume fraction is then defined as follows:

$$f_t = f_n + f_g + f_{sh} \quad (12)$$

Void coalescence is described following the original GTN model using an effective porosity  $f^* \geq f_t$  expressed as:

$$f^* = \begin{cases} f_t & \text{if } f_t < f_c \\ f_c + \frac{f_u - f_c}{f_r - f_c}(f_t - f_c) & \text{if } f_t \geq f_c \end{cases} \quad (13)$$

where  $f_c$  is a critical value corresponding to the onset of coalescence. Parameter  $f_r$  is the value of  $f_t$  at fracture and  $f_u$  is the value of  $f^*$  at fracture. The GTN model uses a yield criterion accounting for the effect of damage and pressure which is expressed as:

$$\phi = \underbrace{\left(\frac{\bar{\sigma}}{\sigma_F}\right)^2 - 1}_{\text{Plasticity}} + \underbrace{2q_1 f^* \cosh\left(\frac{q_2}{2} \frac{\text{Tr}(\bar{\sigma})}{\sigma_F}\right) - (q_1 f^*)^2}_{\text{Effect of cavities}} \quad (14)$$

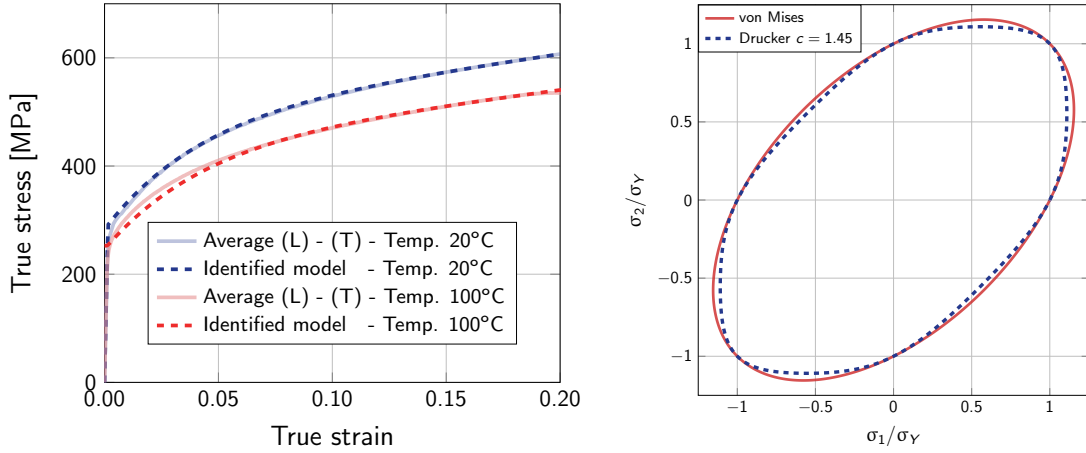
where  $\bar{\sigma}$  is the Drucker equivalent stress which is introduced in the GTN yield surface following [43] instead of the von Mises stress,  $\sigma_F$  is the flow stress described in section 4,  $q_1$  and  $q_2$  are model parameters to be identified.

## 6. Parameter identification

Geometries and velocities used for the identification procedure are given in tab. 2 and marked with a yellow star ★ (for plasticity) and blue star ★ (for damage). Remaining experimental results on different specimens at different loading rates are used in section 7 for the evaluation of the model prediction capability. As the model has many parameters, they are determined stepwise following the strategy which is described in the following. All optimized parameters are gathered in tab. 3.

### 6.1. Work hardening and thermal softening

The hardening law (eq. (1)) is first adjusted. The initial yield stress  $R_e$  is set to the average of the experimental results for quasi-static tensile test on standard flat specimens ( $\dot{\epsilon} = 0.001 \text{ s}^{-1}$ ) along L and T directions at room temperature:  $R_e = 283 \text{ MPa}$  (fig. 5a). The other parameters are identified on the same average curve, using a least square optimization Python script for plastic strains between 0% and 20% (which is slightly below the strain at necking). The following parameters are obtained:  $H = 587 \text{ MPa}$ ,



(a) Identification of the thermal softening part of the model on standard flat specimens

(b) Identified plastic yield criterion.

**Figure 10:** Identification of plasticity model.

$Q = 208$  MPa and  $b = 23.9$ . From the result of this identification the evolution of the true stress in [fig. 10a](#) is plotted as a function of the true strain.

Parameter  $\mu$  describing thermal softening ([eq. \(5\)](#)) can then be easily identified using the quasi-static stress—strain curves obtained at at  $100^\circ\text{C}$  which corresponds to the level of observed temperature increase. Identification (Python script) leads to a value of  $\mu$  equal to  $0.00134$   $^\circ\text{C}^{-1}$ . Note that this value is close to the value proposed by Zhao [4] for a similar material used in the automotive industry. Experiments and simulations are compared in [fig. 10a](#) with good agreement.

## 6.2. Yield surface

The yield surface is then adjusted. The identification is made using Z-opt optimization software [36]. The simulated load—displacement curves are compared with the average (L and T) quasi-static results obtained on NT1, NT2, V45 and M—shape specimens (see [fig. 8](#)). These specimens are particularly relevant for this identification as they allow generating stress states close to shear (M—shape) and between uniaxial tension and plane strain (in particular V45 specimen is close to plane strain along the specimen width direction). The flow stress  $\sigma_F$  is taken equal to  $R(p)$  ([eq. \(1\)](#)) as rate effects can be neglected for those tests. The identified parameter is  $c = 1.45$ . This result indicates that a classical Mises yield surface ( $c = 0$ ) is not sufficient to well represent the yield surface for this material. The obtained yield surface is shown in [fig. 10b](#) where it is compared to the corresponding von Mises surface.

## 6.3. Johnson—Cook law

The Johnson—Cook law ([eq. \(4\)](#)) is then adjusted using the tensile test results on large and standard flat specimens at different loading rates. The value of  $\dot{\epsilon}_0$  is chosen as the maximum strain rate for which the material shows an inviscid response:  $\dot{\epsilon}_0 = 0.00361$   $\text{s}^{-1}$ . The expression of the Johnson-Cook's rate-dependency equation indicates that parameter  $C$  corresponds to the slope of the  $\sigma_F - \langle \ln p / \dot{\epsilon}_0 \rangle_+$  curves for a given plastic strain level. Using this observation, parameter  $C$  is identified with a Python least

square optimization script for plastic strain values contained between 2% and 15%. Considering the self-heating model based on the conversion of plastic work [5] presented above (eq. (6)), this low level of plasticity makes it possible to neglect the small increase of temperature (about 20°C) at high velocity. The identification (see fig. 11a) leads to  $C = 0.0236$ . The stress—strain curves obtained with this parameter are in good agreement with experimental results (see fig. 11b). Thus, in this case the Johnson–Cook model is considered as satisfactory.

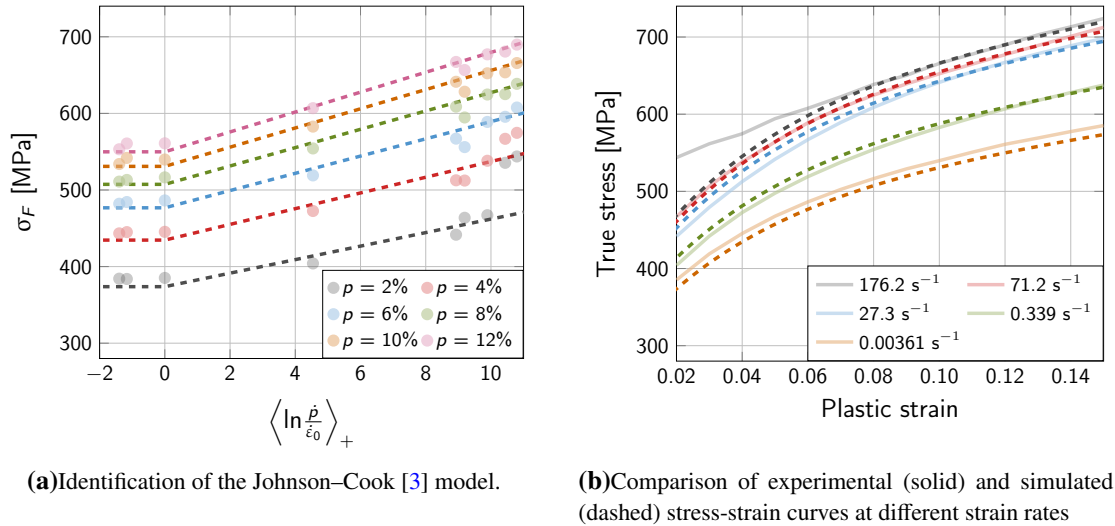


**Figure 11:** Identification of the strain rate dependence model: comparison with test results.

#### 6.4. Damage parameters

Identification of the damage model (section 5) can be simplified by choosing values from the literature. The yield function parameters are taken from [44] as  $q_1 = 1.5$  and  $q_2 = 1.0$ . Parameter  $f_u$  is equal to  $1/q_1$ . Remaining parameters to identify are  $\varepsilon_d$ ,  $A$ ,  $k_w$ ,  $f_c$  and  $f_r$ . Two specimens are used for this identification: the NT1 notched specimen which is representative of high stress triaxiality specimens and the M-shape shear specimen for low stress triaxiality. The shear specimen is particularly important to identify the Nahshon and Hutchinson (N&H) coefficient  $k_w$ . Note therefore that only two specimens were required for the identification of the damage parameters. This was possible because for the two selected specimens, stress states differ and also because both crack initiation and propagation are considered in the identification procedure thanks to the stable load decrease for the NT1 specimen. Quasi-static loadings are preferred to avoid any thermal effect on softening. Since damage models are well known to be mesh-dependent because of stress softening and damage localization [45], the parameters have to be identified for a fixed mesh size which will represent the width of the damage localization band. It is then chosen to fix the mesh size  $L_e$  at one sixth of the sheet thickness (6 hexahedral elements in the thickness),  $L_e \approx 0.2$  mm. Using the Z-opt software, identification is realised using NT1 and M-shape specimens (see fig. 12). The experimental loading rate is applied (respectively  $0.002 \text{ mm.s}^{-1}$  and  $0.003 \text{ mm.s}^{-1}$ ) at room temperature. Simulations were automatically carried out by the optimization software up to full failure in order to match the entire load—displacement curves. Each iteration lasted about 1 hour. The optimized values are:  $\varepsilon_d = 0.3$ ,  $A = 0.11$ ,  $k_w = 2.65$ ,  $f_c = 0.16$  and  $f_r = 0.2$ . Note that if the Nahshon and Hutchinson modification is

deactivated ( $k_w = 0$ ), the failure of M-shape specimen cannot be predicted (see fig. 12b). A slight difference is observed on NT1 results (see fig. 12a) because of quasi plane strain conditions encountered in the center of the specimen.

Finally a mesh size sensitivity analysis was carried out. It is concluded that a good fit can still be obtained when changing the mesh by only modifying the nucleation rate  $A$  proportionally to the new mesh size ( $L'_e$ ) as:  $A \rightarrow A' = A(L'_e/L_e)$ . This simple rule can however only be applied for  $L'_e < 0.5$  mm. Above this mesh size, the strain gradient is no longer well described so that M-shape, V45 and CCP specimens cannot be properly simulated as gradients are very steep in these specimens.

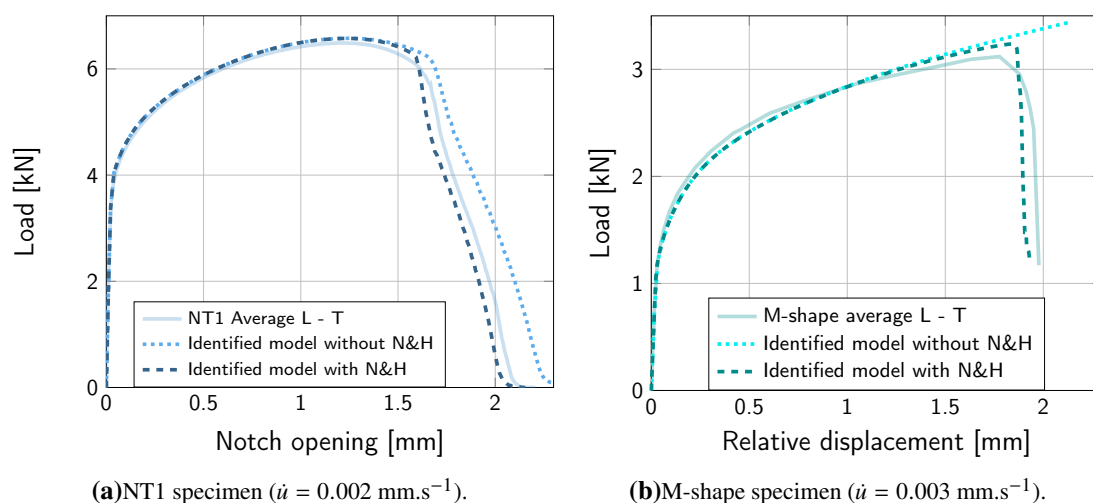


**Figure 12:** Damage model identification results obtained with Z-opt with a mesh size of  $L_e = 0.2$  mm.

### 6.5. Damage at high loading rates and self-heating

To simulate dynamic tests, it is assumed that damage parameters are temperature and strain rate independent. When using the GTN growth model, this assumption implies [46] that ductility for a given stress state is also temperature and strain rate independent as growth rate depends on a stress ratio (stress triaxiality) which remains constant. Nucleation could be affected by the stress level [47] but this possible effect was not accounted for in this study. Assuming strain controlled nucleation leads again to temperature and strain rate independent damage rates. Therefore assuming that damage parameters are temperature and strain rate independent, implies that damage mechanisms are assumed to remain similar (in the present case mainly ferrite/martensite decohesion and subsequent moderate void growth) and to keep the same rate dependence with respect to temperature and strain rate. In that case, local (material point) ductility remains unchanged. However, adiabatic heating (a softening mechanism) will favor earlier strain localization and therefore reduce the macroscopic ductility. Using these assumptions it is for instance possible to well describe the dynamic Charpy tests [48, 49]. These assumption would however not be valid for instance in the case of dynamic strain aging (DSA) which is known to reduce ductility in the case of duplex steels [50] (above  $150^\circ\text{C}$  in this reference). In that case it would be necessary to have damage parameters depending on temperature and/or strain rate. In the present case, the model will overestimate ductility for quasi-static tests conducted at  $100^\circ\text{C}$  (fig. 7). In this study, these tests were in fact conducted to characterize the temperature

dependence of the flow stress only (parameter  $\mu$  in eq. (5)). The assumptions made here will be validated in the next section where all tests (quasi-static and dynamic) carried out at room temperature are simulated.

The value of the Taylor–Quinney coefficient is taken from [6] and set to  $\eta_k = 0.9$ . Thermal properties of DP450 steel are assumed to be close to those of DP590, thus corresponding material parameters  $\rho=7850 \text{ kg.m}^{-3}$ , and  $C_p=420 \text{ J.kg}^{-1}.\text{°C}^{-1}$ , proposed in [6], are also taken. The  $\omega$  function is then fitted so as to reproduce gradual softening observed during high velocity tests. It is not fitted on temperature measurements but computed temperature increase is qualitatively in agreement with estimates obtained with the infrared camera (see fig. 18 below). The identification of the  $\omega$  function (eq. (6)) needs therefore to be performed after the identification of the damage parameters on quasi-static tests (see 6.4). Roth and Mohr [6] have proposed to set  $\dot{\epsilon}_{is} = \dot{\epsilon}_0$ . Using this assumption (which would simplify the identification procedure) did not allow to obtain a good fit of the database and consequently  $\dot{\epsilon}_{is}$  was also tuned. As self-heating only affects the macroscopic response when the entire specimen cross-section undergoes temperature increase, large flat tensile specimens are used for the identification of  $\dot{\epsilon}_{is}=0.002 \text{ s}^{-1}$  and  $\dot{\epsilon}_{ad}=0.04 \text{ s}^{-1}$ . This fit was validated on FN specimens which also show almost uniform self-heating. Identification requires to simulate the entire specimens so that an automatic optimisation software must be used (Z-opt in this case). Comparison of experiments and simulations are shown in fig. 13 with reasonable agreement.

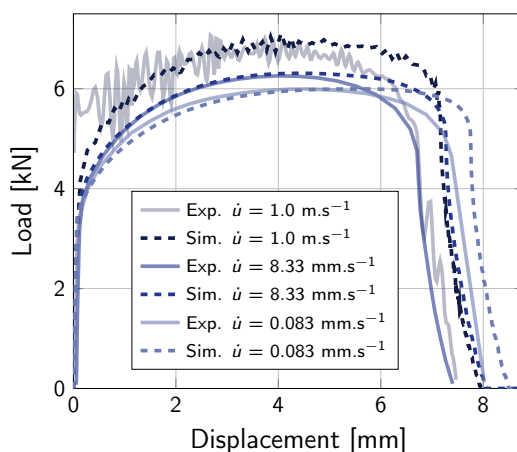


**Figure 13:** Identification of the self-heating part of the model on large flat specimens.

## 7. Simulation of the database and validation of the model

In this last section, the constitutive model is implemented in the finite element software Z-set to perform simulations of several quasi-static and dynamic tests. Experiments and simulations are systematically compared to evaluate the prediction capability of the proposed model.

### 7.1. Numerical methods

To perform simulations of the various test specimens, the constitutive model is implemented following a fully implicit scheme in the Z-set object oriented finite element software [51, 52]. This implementation is realized using the formalism proposed by Besson *et al.* [53]. The simulations are realized using regular

$E$ [GPa]	$\nu$	$R_e$ [MPa]	$H$ [MPa]	$Q$ [MPa]	$b$	$c$
192.0	0.3	283.0	587.0	208.0	23.9	1.45
$\dot{\epsilon}_0$ [ $s^{-1}$ ]	$C$	$\mu$ [ $^{\circ}C^{-1}$ ]	$\eta_k$	$\rho$ [ $kg.m^{-3}$ ]	$C_p$ [ $J.kg^{-1}.^{\circ}C^{-1}$ ]	$\dot{\epsilon}_{is}$ [ $s^{-1}$ ]
0.00361	0.0236	0.00134	0.9	7850.0	420.0	0.002
$\dot{\epsilon}_{ad}$ [ $s^{-1}$ ]	$\epsilon_d$	$A$	$k_w$	$f_c$	$f_r$	$f_u$
0.04	0.3	0.11	2.65	0.16	0.2	$1/q_1$
$q_1$	$q_2$	$L_e$				
1.5	1.0	0.2 [mm]				

**Table 3:** Identified parameters for a fixed mesh size of  $L_e = 0.2$  mm.

meshes with a relatively constant mesh size of  $L_e = 0.2$  mm. These meshes consist in 8-node brick elements with full integration (8 Gauss points). To avoid pressure fluctuations within the elements, selective integration technique [54] is used. It is emphasized that, in all cases, damage maximum values are localized on one row of Gauss points illustrating damage localization responsible for mesh size dependency. For this reason, it is important to keep a constant mesh size in the crack propagation zone.

Usual symmetry conditions are used so that 1/2 of the specimens is meshed (half thickness). Other symmetries are not accounted for so as to be able to represent non-symmetric crack paths experimentally observed for M-shape and FN specimens. For all simulations, the damage variable  $f_t$  field during or after full failure is plotted with the same scale as presented in fig. 14c. Considering the identified parameters (see tab. 3), element rupture is obtained for  $f_t = f_r = 0.20$ . Ruptured elements are removed from the calculation. To avoid getting a singular global stiffness matrix, displacement increments at nodes belonging only to removed elements are then fixed. Quasi-static tests are simulated using a static implicit scheme. Dynamic tests are simulated using a dynamic implicit numerical solver to consider inertia effects on the specimen response.

## 7.2. Quasi-static tests

Quasi-static simulations at room temperature are first presented and results are shown in fig. 14 (standard flat, NT1, NT2), fig. 15 (V45, Central hole, M-shape) and fig. 16 (CCP, FN). An overall good prediction is observed for all specimens. For load—displacement curves, experimental scatter is represented by the filled area; this scatter corresponds to both material anisotropy and actual scatter (which is very limited). Experimental macroscopic transverse strains curves obtained by shadow tracking (see fig. 4) are also compared in fig. 14b, fig. 14e, fig. 14h, fig. 15b, fig. 15e. In cases where cracks are initiated at the notch root, transverse strains can only be evaluated before the onset of cracking as the shadow tracking technique is not accurate enough to detect the crack tip. This situation prevails in all cases except for the standard flat specimens in which cracks are initiated at the center of the specimen. The difference between simulation and experiment for the V45 specimens (fig. 15b) is attributed to an underestimation of the transverse strain. For this specimen, transverse strain before crack initiation is very small ( $\simeq 1.3\%$ ) so that the shadow tracking is not accurate enough.

In all cases a very good agreement is obtained between simulated and experimental load—displacement/notch opening curves up to full specimen failure (*i.e.* load = 0). This first shows that the

hardening model is appropriately identified even for strain levels larger than the necking as shown, for instance, in [fig. 14b](#) where the engineering stress is plotted as a function of the transverse strain. In all cases, loads and macroscopic transverse strains are well predicted. Crack initiation location is also well represented; in particular initiation at the center of the specimen for standard flat specimens is well captured by the model (see [fig. 14c](#)).

M-shape simulated failure given in [fig. 15h](#) occurs at one of the two sheared ligaments as observed experimentally. This disymmetric behavior is attributed to small differences between both side of the mesh and numerical errors. These small differences are increased due to the intrinsic softening character of the constitutive equations thus leading to a disymmetric response.

The CCP specimen, which is representative of long crack propagation, is also well represented (see [fig. 16a](#) and [fig. 16b](#)). Its overall behavior is close to that of the V45 specimen.

Due to its geometry, four crack initiation spots exist in the FN specimen. This lead to crack path dissymmetry and to various possible paths as exemplified in [fig. 16d](#) and [fig. 16g](#). This is attributed to slightly different applied boundary conditions (due to *e.g.* a small misalignment in the griping system or specimen positioning). Note that, these differences are small enough so as to have no influence on the macroscopic load—displacement curves. To account for this experimental scatter, displacements measured using DIC were used as boundary conditions on horizontal lines located at  $\pm 17.5$  mm from the center line of the specimens. This is done using the *Escale* software [55] which allows dialog between experiments and simulations. The simulation is then able to represent the corresponding crack paths of FN specimen in tests carried out at different slow loading rates of  $0.009 \text{ mm}\cdot\text{s}^{-1}$  and  $0.09 \text{ mm}\cdot\text{s}^{-1}$  (see respectively [fig. 16e](#) and [fig. 16h](#)). One can notice that the corresponding load—displacement curves given in [fig. 16c](#) and [fig. 16f](#) are also well reproduced. As already discussed above (6.5), the model is however unable to reproduce to ductility loss observed at  $100^\circ\text{C}$  under quasi-static conditions in [fig. 7](#). In that case, the model predicts a constant ductility. The ductility loss might be due to dynamic strain aging which was shown to reduce ductility [50]. Its possible effect is not integrated in the present model. Note that these loading conditions do not correspond to car crash situation.

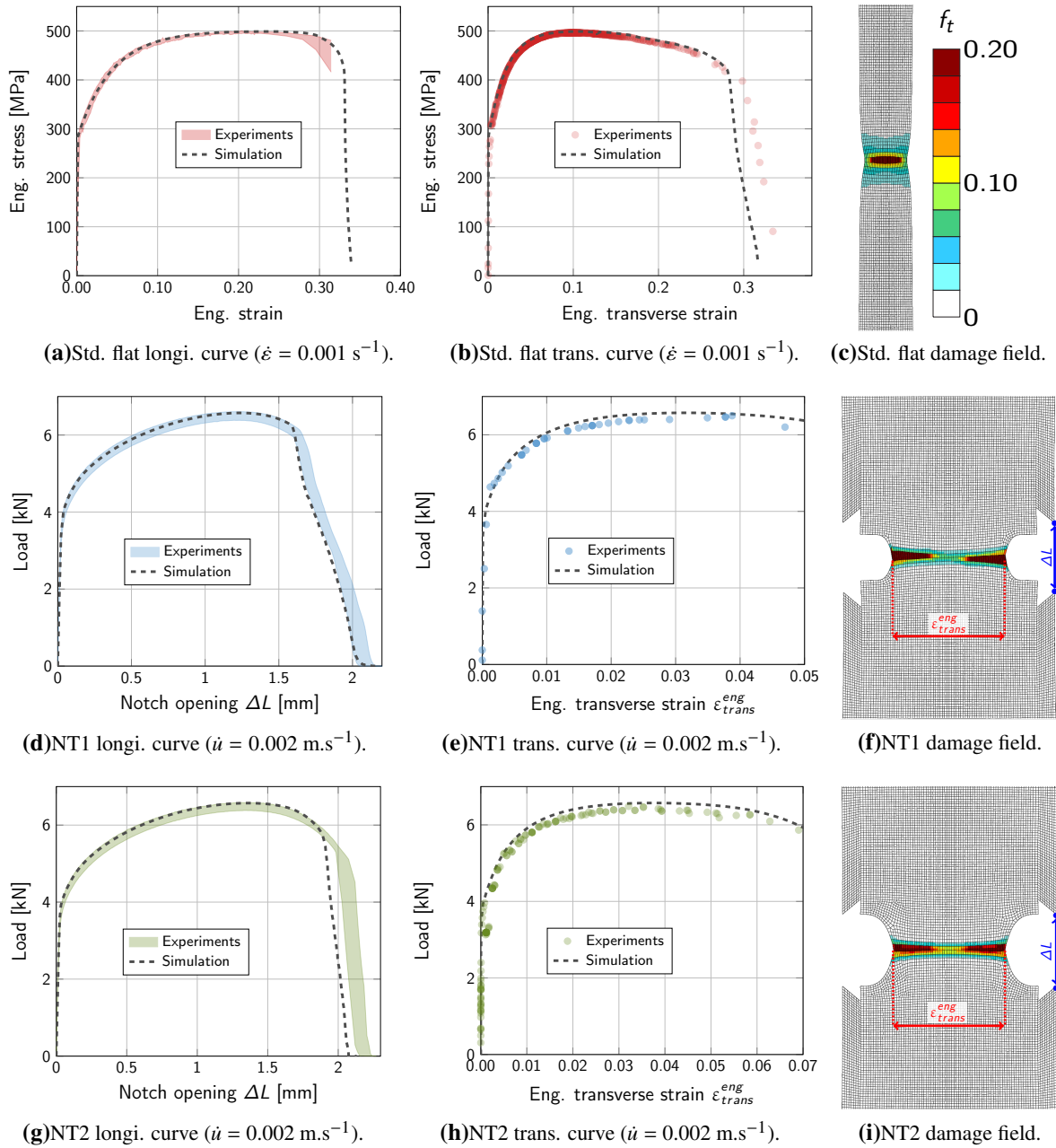


**Figure 14:** Comparison between simulation and quasi-static tensile tests - part I.

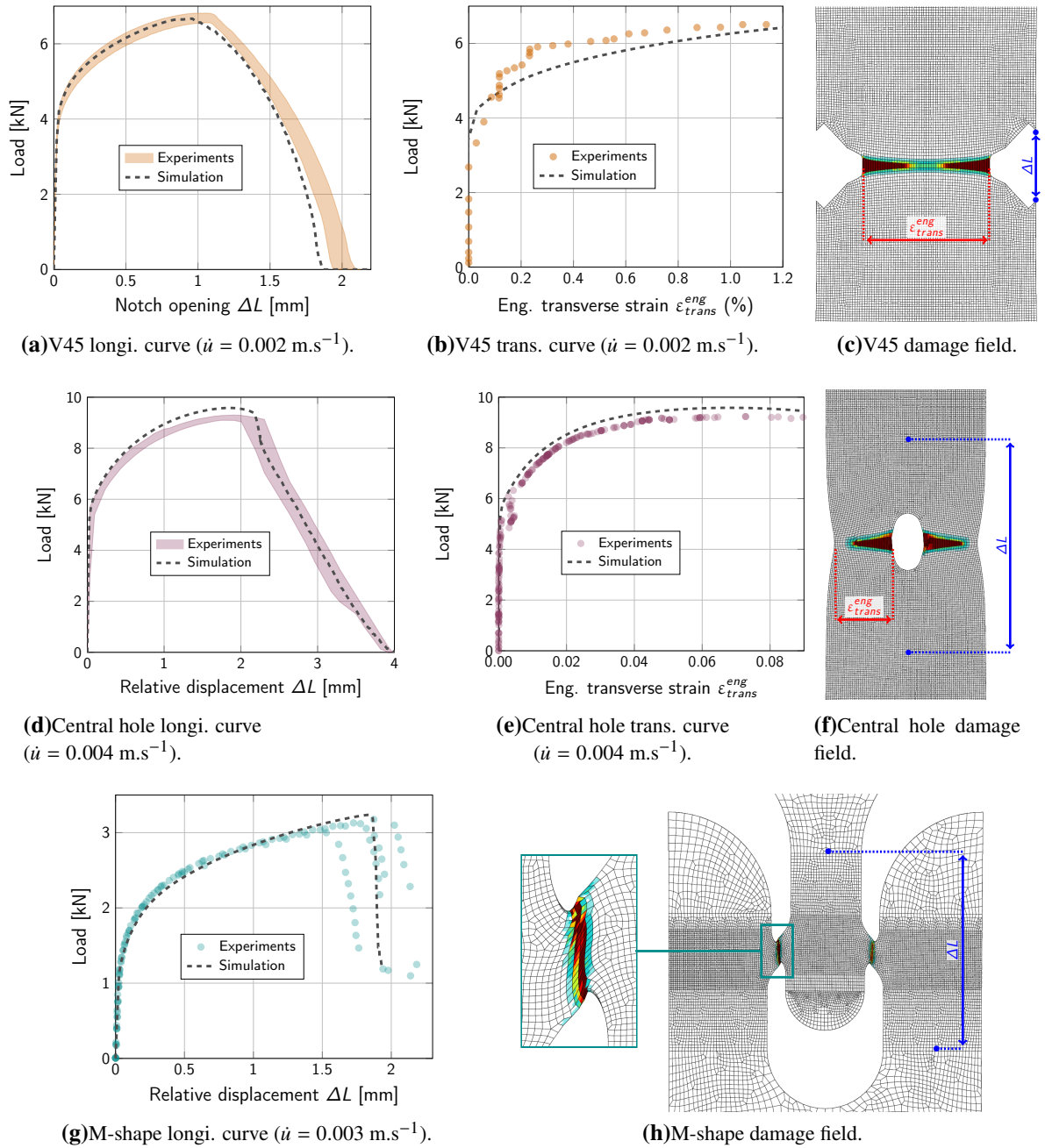
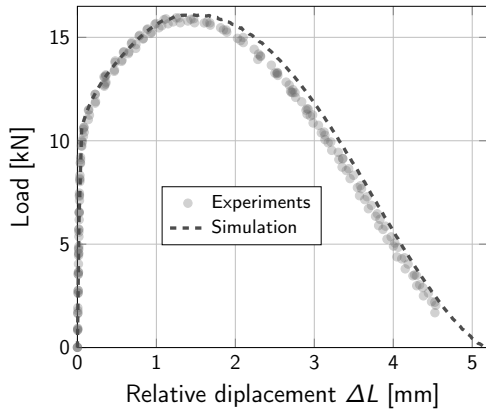
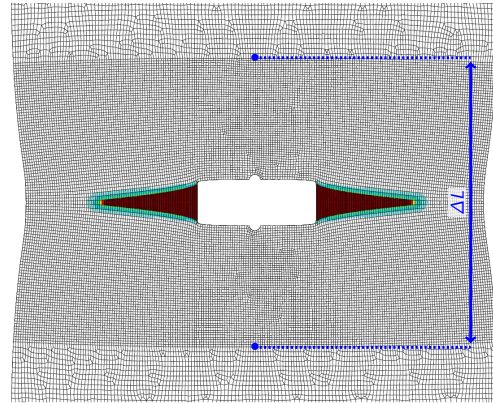


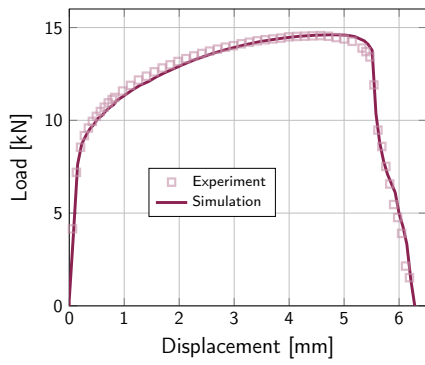
**Figure 15:** Comparison between simulation and quasi-static tensile tests - part II.



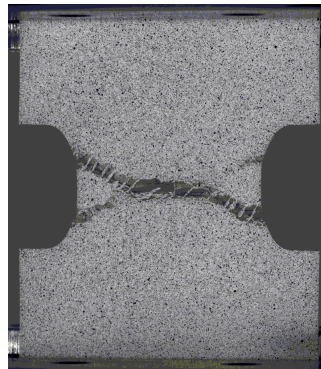
(a) CCP longitudinal curve ( $\dot{u} = 0.004 \text{ m.s}^{-1}$ ).



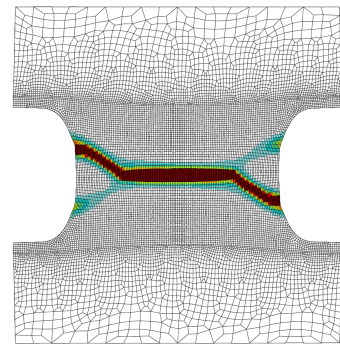
(b) CCP damage field.



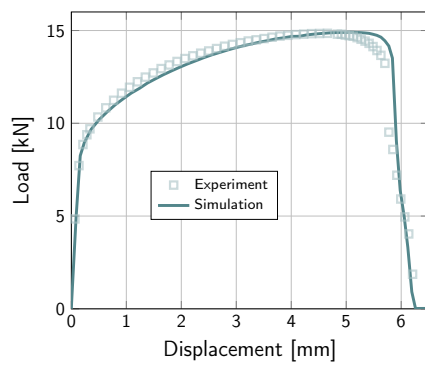
(c) FN longi. curve ( $\dot{u} = 0.009 \text{ m.s}^{-1}$ ).



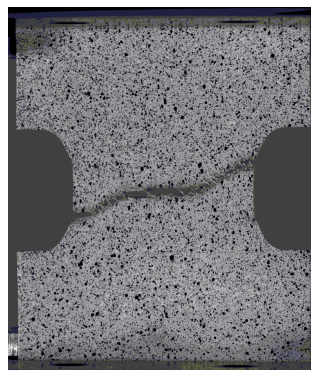
(d) FN final state ( $\dot{u} = 0.009 \text{ m.s}^{-1}$ ).



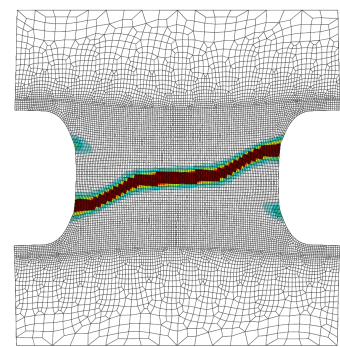
(e) FN damage field ( $\dot{u} = 0.009 \text{ m.s}^{-1}$ ).



(f) FN longi. curve ( $\dot{u} = 0.09 \text{ m.s}^{-1}$ ).



(g) FN final state ( $\dot{u} = 0.09 \text{ m.s}^{-1}$ ).



(h) FN damage field ( $\dot{u} = 0.09 \text{ m.s}^{-1}$ ).

**Figure 16:** Comparison between simulation and quasi-static tensile tests - part III.

### 7.3. Dynamic tests

Dynamic tests are then simulated and results are given in [fig. 17](#). These results also show an overall good prediction of strength levels and displacements at failure for all specimens. Note that, for the sake of clarity, only few loading rates are presented. No transverse strain measurements were performed during dynamic tests. Quasi-static results are also plotted for comparison.

The simulated stress-strain curves at different plastic strain rates (see [fig. 17a](#)) well represent the increase of strength due to viscous effects. The slight stress decrease observed at high strain rates (see the yellow frame) is caused by self-heating which is well reproduced by the simulation. A similar trend was observed in [\[6\]](#) for flat tensile specimens. Large flat specimens were used for the identification of Roth and Mohr self-heating parameters and are already presented above in [fig. 13](#). Results illustrate the macroscopic loss of ductility with the increasing loading rates which is quite well reproduced by the model. The corresponding simulated temperature fields (see [fig. 18](#)) are also in good agreement with infrared pictures. A slightly higher simulated temperature is however observed in the fracture areas. These results also validate the assumption that it is not necessary to model the effect of temperature on damage development in the case of dynamic tests conducted at room temperature.

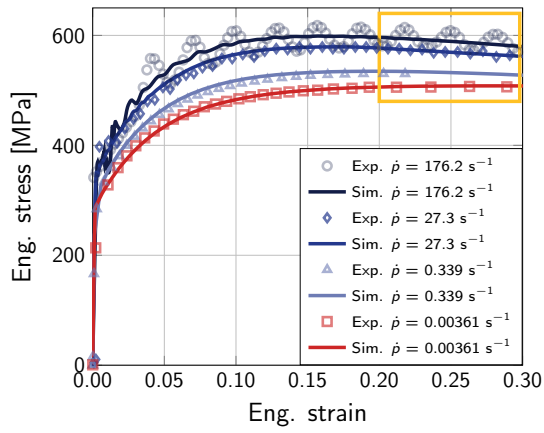
Notched specimen NT1 (see [fig. 17b](#)) and V45 (see [fig. 17c](#)) are less sensitive to self-heating. Plastic strain being localized in the thin notched area, heat generation does not affect the entire specimen cross section and is not visible on the macroscopic response. Ductility is thus quasi-constant for all loading rates on these geometries. This behavior is also well represented by the model. The same observation is valid for CCP dyna. tests (see [fig. 17d](#)). Note that for this specimen, the level of strength for the fastest loading rate of  $7.0 \text{ m.s}^{-1}$  is slightly underestimated.

M-shape specimens are less ductile at high loading rates (see [fig. 17e](#)). This is consistent with results on tensile tests as the entire sheared areas are uniformly strained so that the entire cross section is submitted to heating. Localization is therefore favoured compared to quasi-static loading so that failure occurs earlier.

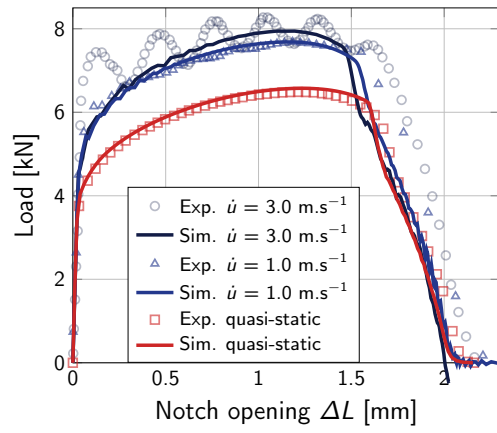
FN specimens are simulated for two fast loading rates equal  $8.33 \text{ mm.s}^{-1}$  and  $1.0 \text{ m.s}^{-1}$ . Both show different levels of strength and displacement at failure. The specimen simulated responses well represent the material resistance level increase and the loss of macroscopic ductility due to thermal effects. Due to the inability to perform DIC analyses at high velocities, the accurate boundary conditions could not be applied for these simulations. This can explain the slight difference between the experimental and simulated elastic responses. Nevertheless, a good general agreement with experiments is still observed.

## 8. Conclusion

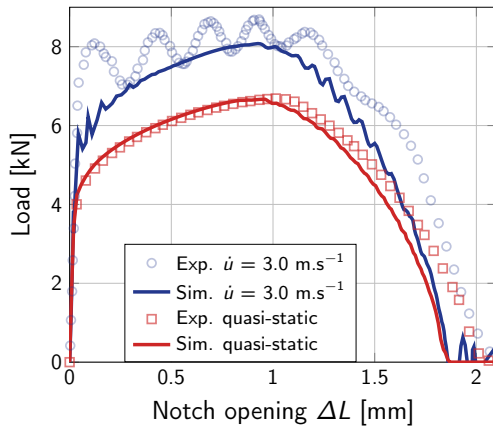
To overcome the shortcomings of fracture criteria for ductile cracking prediction in car simulations, a Gurson type damage model was proposed and evaluated. First of all, a very comprehensive experimental campaign allowed to observe the material response and to understand the phenomena involved in DP450 steel failure. These phenomena were modelled using an original set of constitutive equations with a limited number of parameters to identify. A practical identification procedure was proposed. It should be noted that the identification of the damage parameters, requires only a small number of tensile tests on relevant geometries, which is an advantage for industrial use. At last, the proposed model and fitted parameters were validated based on tests that were not used for the identification. Comparisons between tests and simulations for different stress states and loading rates have shown that the model is able to predict both the macroscopic response of the specimens in terms of load—displacement curves and the crack path, with good accuracy.



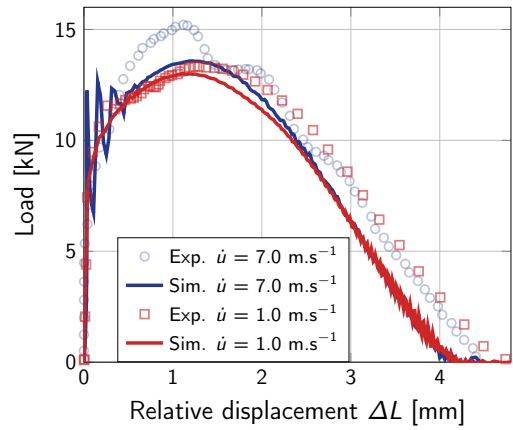
(a) Dynamic stress-strain curves.



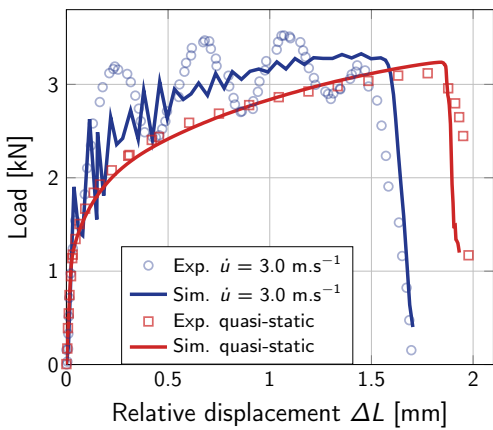
(b) NT1 dynamic longitudinal curves.



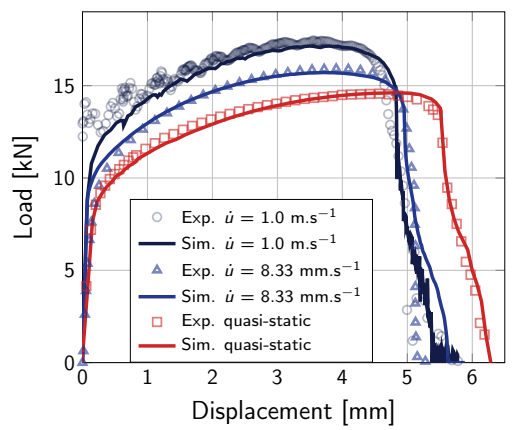
(c) V45 dynamic longitudinal curves.



(d) CCP dyna. longitudinal curves.



(e) M-shape dynamic longitudinal curves.



(f) FN dynamic longitudinal curves.

**Figure 17:** Comparison between simulation and dynamic tensile tests.

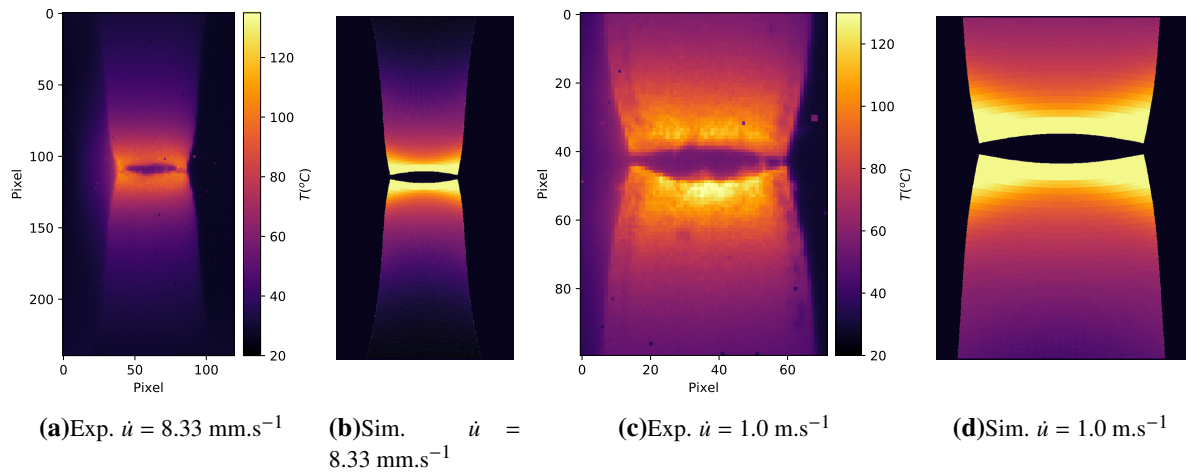


**Figure 18:** Comparison between experimental and simulated temperature fields on Large flat specimen.

However, some improvements are still required to ensure a reliable crack prediction usable in automotive industry. First, crash simulations are mostly performed using dynamic explicit finite element codes more convenient for strongly non-linear problems and fast transients. It is then considered to implement the proposed constitutive model into the Europlexus [56] solver. As explicit solvers require numerous very small time increments, it is proposed to use an explicit integration scheme for the constitutive equations following the NICE (“Next Increment Correct Error”) algorithm proposed by Halilović *et al.* [11] so as to obtain a computationally efficient code. Note that to predict cracking at material scale, a very small mesh size is used in this paper. However the stability condition of dynamic explicit codes implies that the smaller the mesh size, the smaller the time step. The small mesh used in this study could therefore lead to prohibitive computational costs in large structural simulations. A possible solution could be to refit the material parameters for a larger given mesh size. However, representing the entire database using this solution could become difficult.

Further studies will focus on remedying mesh dependency of the results. Indeed, it is important to note that due to stress-softening, the problem becomes ill posed and damage is finally localized in the smallest band that can be captured by the mesh. Thus, once the parameters have been identified for a given mesh size, all the simulations must be performed with the same mesh size. Besides, although that was not observed with the present results, it is well known that in some cases, coupled damage models might also be dependent to mesh orientation [45]. And yet, since car parts can have very complex geometries modelled with the use of meshes mixing hexahedra/prismes (3D continuous elements) or triangles/quadrangles (shell elements), it is impossible to ensure a uniform mesh size or mesh orientation. A possible solution to ensure mesh-independent results could be to regularize the problem. A recently proposed non-local approach [57] compatible with dynamic explicit scheme could be for example considered. These models introduce an intrinsic material length scale so that below a given element size, results become mesh independent.

## Acknowledgment

The Groupe PSA is gratefully acknowledged for providing and supporting this research opportunity. Mr Remy Bompont, is acknowledged for his guidance and for providing the DP450 steel material. Mr

Laurent Di Valentin is acknowledged as well for his advice and enthusiasm about the work already made. The French Aerospace Lab. Onera is also gratefully acknowledged for supervising, expertising and for providing the numerical resources. Dr David Levêque and Dr Thomas Fourest are especially thanked for the experimental support. Finally, the Centre des Matériaux Mines ParisTech is also acknowledged for the machining and experimental resources.

## References

- [1] E. Voce, [The Relationship between Stress and Strain for Homogeneous Deformation](#), Journal of the Institute of Metals 74 (1948) 537–562 (1948).  
URL <https://ci.nii.ac.jp/naid/10026664078/en/>
- [2] D. Drucker, B. U. D. o. A. Mathematics, U. S. O. o. N. Research, U. S. N. D. B. o. Ships, [The Relation of Experiments to Mathematical Theories of Plasticity](#), Technical report (Brown University. Division of Applied Mathematics), Division of Applied Mathematics, Brown University, 1948 (1948).  
URL <https://books.google.fr/books?id=srvkHAAACAAJ>
- [3] G. R. Johnson, W. H. Cook, A constitutive model and data for metals subjected to large strains, high strain rates and high temperatures, in: Proceedings of the 7th International Symposium on Ballistics, Vol. 21, The Hague, The Netherlands, 1983, pp. 541–547 (1983).
- [4] H. Zhao, [A constitutive model for metals over a large range of strain rates identification for mild-steel and aluminium sheets](#), Materials Science and Engineering: A 230 (1-2) (1997) 95–99 (1997).  
URL <http://www.sciencedirect.com/science/article/pii/S0921509397000245>
- [5] G. I. Taylor, H. Quinney, The latent energy remaining in a metal after cold working, Proceedings of the Royal Society of London. Series A, Containing Papers of a Mathematical and Physical Character 143 (849) (1934) 307–326 (1934). doi: [10.1098/rspa.1934.0004](https://doi.org/10.1098/rspa.1934.0004).
- [6] C. C. Roth, D. Mohr, [Effect of strain rate on ductile fracture initiation in advanced high strength steel sheets: Experiments and modeling](#), International Journal of Plasticity 56 (2014) 19–44 (May 2014). doi: [10.1016/j.ijplas.2014.01.003](https://doi.org/10.1016/j.ijplas.2014.01.003).  
URL <http://linkinghub.elsevier.com/retrieve/pii/S0749641914000047>
- [7] K. Nahshon, J. Hutchinson, [Modification of the Gurson Model for shear failure](#), European Journal of Mechanics - A/Solids 27 (1) (2008) 1–17 (Jan. 2008). doi: [10.1016/j.euromechsol.2007.08.002](https://doi.org/10.1016/j.euromechsol.2007.08.002).  
URL <http://linkinghub.elsevier.com/retrieve/pii/S0997753807000721>
- [8] A. L. Gurson, others, [Continuum theory of ductile rupture by void nucleation and growth: Part I—Yield criteria and flow rules for porous ductile media](#), Journal of engineering materials and technology 99 (1) (1977) 2–15 (1977).  
URL <http://materialstechnology.asmedigitalcollection.asme.org/pdfaccess.ashx?ResourceID=4461789&PDFSource=13>
- [9] V. Tvergaard, [Influence of voids on shear band instabilities under plane strain conditions](#), International Journal of Fracture 17 (4) (1981) 389–407 (1981).  
URL <http://link.springer.com/article/10.1007/BF00036191>
- [10] V. Tvergaard, A. Needleman, DCAMM., DTH., [Analysis of the Cup-cone Fracture in a Round Tensile Bar](#), Lyngby. Technical university of Denmark, Danish center for applied mathematics and mechanics. Report, Technical University of Denmark, 1983 (1983).  
URL <https://books.google.fr/books?id=HzuDPgAACAAJ>
- [11] M. Halilović, M. Vrh, B. Štok, [NICE h : a higher-order explicit numerical scheme for integration of constitutive models in plasticity](#), Engineering with Computers 29 (1) (2013) 55–70 (Jan. 2013). doi: [10.1007/s00366-011-0243-9](https://doi.org/10.1007/s00366-011-0243-9).  
URL <http://link.springer.com/10.1007/s00366-011-0243-9>
- [12] J. R. Rice, D. M. Tracey, On the ductile enlargement of voids in triaxial stress fields, Journal of the Mechanics and Physics of Solids 17 (3) (1969) 201–217 (1969).
- [13] G. R. Johnson, W. H. Cook, [Fracture characteristics of three metals subjected to various strains, strain rates, temperatures and pressures](#), Engineering Fracture Mechanics 21 (1) (1985) 31 – 48 (1985). doi: [http://dx.doi.org/10.1016/0013-7944\(85\)90052-9](https://doi.org/http://dx.doi.org/10.1016/0013-7944(85)90052-9).  
URL <http://www.sciencedirect.com/science/article/pii/0013794485900529>
- [14] Y. Bai, T. Wierzbicki, [Application of extended Mohr–Coulomb criterion to ductile fracture](#), International Journal of

- Fracture 161 (1) (2010) 1–20 (Jan. 2010). doi:10.1007/s10704-009-9422-8.  
URL <http://link.springer.com/10.1007/s10704-009-9422-8>
- [15] C. A. Coulomb, Essai sur une application des r gles de maximis & minimis   quelques probl mes de statique, relatifs   l'architecture, De l'Imprimerie Royale, Paris, 1776 (1776).
- [16] O. Mohr, Abhandlungen aus dem Gebiete der technischen Mechanik, W. Ernst & Sohn, Berlin, 1914 (1914).
- [17] D. Mohr, S. J. Marcadet, **Micromechanically-motivated phenomenological Hosford-Coulomb model for predicting ductile fracture initiation at low stress triaxialities**, International Journal of Solids and Structures 67-68 (2015) 40–55 (Aug. 2015). doi:10.1016/j.ijsolstr.2015.02.024.  
URL <http://linkinghub.elsevier.com/retrieve/pii/S0020768315000700>
- [18] A. Hershey, The plasticity of an isotropic aggregate of anisotropic face centered cubic crystals, J. Appl. Mech. 21 (3) (1954) 241 – 289 (1954).
- [19] W. F. Hosford, **A Generalized Isotropic Yield Criterion**, Journal of Applied Mechanics 39 (2) (1972) 607–609 (Jun. 1972). doi:10.1115/1.3422732.  
URL <http://dx.doi.org/10.1115/1.3422732>
- [20] H. Tresca, **M moire sur l' coulement des corps solides soumis   de fortes pressions**, Gauthier-Villars, 1864 (1864).  
URL <https://books.google.fr/books?id=4hP9mAECAAJ>
- [21] K. Pack, D. Mohr, **Combined necking & fracture model to predict ductile failure with shell finite elements**, Engineering Fracture Mechanics 182 (2017) 32–51 (Sep. 2017). doi:10.1016/j.engfracmech.2017.06.025.  
URL <http://www.sciencedirect.com/science/article/pii/S0013794416305112>
- [22] K. Pack, T. Tancogne-Dejean, M. Gorji, D. Mohr, **Hosford-coulomb ductile failure model for shell elements: Experimental identification and validation for dp980 steel and aluminum 6016-t4**, International Journal of Solids and Structures 151 (08 2018). doi:10.1016/j.ijsolstr.2018.08.006.
- [23] A. K. Pickett, T. Pyttel, F. Payen, F. Lauro, N. Petrinic, H. Werner, J. Christlein, **Failure prediction for advanced crashworthiness of transportation vehicles**, International Journal of Impact Engineering 30 (7) (2004) 853–872 (Aug. 2004). doi:10.1016/j.ijimpeng.2004.04.004.  
URL <https://linkinghub.elsevier.com/retrieve/pii/S0734743X04000703>
- [24] A. Ockewitz, D.-Z. Sun, H. Klamser, D. Malcher, **Damage modelling of automobile components of aluminium materials under crash loading**, in: 5. LS-DYNA Anwenderforum 2006, 2006, pp. D-II-1–D-II-11 (2006).
- [25] J. Marzbanrad, S. Norozi, A. Ahmadi, **Damage modeling in crashworthiness of dual-phase steel**, 2013 (May 2013).
- [26] J. Besson, **Continuum models of ductile fracture : A review**, International Journal of Damage Mechanics 19 (2010) 3–52 (2010). doi:10.1177/1056789509103482.  
URL <https://hal.archives-ouvertes.fr/hal-00550957>
- [27] T. S. Cao, **Models for ductile damage and fracture prediction in cold bulk metal forming processes: a review**, International Journal of Material Forming 10 (2) (2017) 139–171 (Apr. 2017). doi:10.1007/s12289-015-1262-7.  
URL <http://link.springer.com/10.1007/s12289-015-1262-7>
- [28] C. Defa sse, M. Mazi re, L. Marcin, J. Besson, **Ductile fracture of an ultra-high strength steel under low to moderate stress triaxiality**, Engineering Fracture Mechanics 194 (2018) 301 – 318 (2018). doi:https://doi.org/10.1016/j.engfracmech.2017.12.035.  
URL <http://www.sciencedirect.com/science/article/pii/S0013794417310147>
- [29] X. Li, C. Roth, D. Mohr, **Machine-learning based temperature- and rate-dependent plasticity model: Application to analysis of fracture experiments on DP steel**, Int. J. Plasticity 118 (2019) 320–344 (2019).
- [30] D. Anderson, S. Winkler, A. Bardelcik, M. Worswick, **Influence of stress triaxiality and strain rate on the failure behavior of a dual-phase DP780 steel**, Materials & design 60 (2014) 198–207 (2014).
- [31] A. Dalloz, J. Besson, A.-F. Gourgues-Lorenzon, T. Sturel, A. Pineau, **Effect of shear cutting on ductility of a dual phase steel**, Engineering Fracture Mechanics 76 (10) (2009) 1411 – 1424, matModels 2007 (2009). doi:https://doi.org/10.1016/j.engfracmech.2008.10.009.  
URL <http://www.sciencedirect.com/science/article/pii/S0013794408002786>
- [32] I. Sarraf, A. Jenab, K. Boyle, D. Green, **Effect of rate-dependent constitutive equations on the tensile flow behaviour of DP600 using Rousselier damage model**, Materials & Design 117 (2017) 267–279 (Mar. 2017). doi:10.1016/j.matdes.2016.12.088.  
URL <http://linkinghub.elsevier.com/retrieve/pii/S0264127516316124>
- [33] N. L. Mao t, S. Thuillier, P. Manach, **Aluminum alloy damage evolution for different strain paths   application to hemming process**, Engineering Fracture Mechanics 76 (9) (2009) 1202 – 1214 (2009). doi:https://doi.org/10.1016/

- [j.engfracmech.2009.01.018](#).  
 URL <http://www.sciencedirect.com/science/article/pii/S001379440900023X>
- [34] R. v. Mises, *Mechanik der festen Körper im plastisch- deformablen Zustand*, Nachrichten von der Gesellschaft der Wissenschaften zu Göttingen, Mathematisch-Physikalische Klasse 1913 (1913) 582–592 (1913).  
 URL <http://eudml.org/doc/58894>
- [35] A. Mendelson, *Plasticity; theory and application*, Macmillan series in applied mechanics, Macmillan, 1968 (1968).  
 URL <https://books.google.fr/books?id=UM9RAAAAMAAJ>
- [36] R. L. Riche, J. Gaudin, J. Besson, *An object-oriented simulation-optimization interface*, Computers & Structures 81 (17) (2003) 1689 – 1701 (2003). doi:[https://doi.org/10.1016/S0045-7949\(03\)00186-X](https://doi.org/10.1016/S0045-7949(03)00186-X).  
 URL <http://www.sciencedirect.com/science/article/pii/S004579490300186X>
- [37] F. J. Zerilli, R. W. Armstrong, *Dislocation mechanics based constitutive relations for material dynamics calculations*, Journal of Applied Physics 61 (5) (1987) 1816–1825 (Mar. 1987). doi:[10.1063/1.338024](https://doi.org/10.1063/1.338024).  
 URL <http://aip.scitation.org/doi/10.1063/1.338024>
- [38] C. C. Chu, A. Needleman, *Void Nucleation Effects in Biaxially Stretched Sheets*, Journal of Engineering Materials and Technology 102 (3) (1980) 249–256 (Jul. 1980). doi:[10.1115/1.3224807](https://doi.org/10.1115/1.3224807).  
 URL <http://dx.doi.org/10.1115/1.3224807>
- [39] K. L. Nielsen, V. Tvergaard, *Ductile shear failure or plug failure of spot welds modelled by modified Gurson model*, Engineering Fracture Mechanics 77 (7) (2010) 1031–1047 (May 2010). doi:[10.1016/j.engfracmech.2010.02.031](https://doi.org/10.1016/j.engfracmech.2010.02.031).  
 URL <http://linkinghub.elsevier.com/retrieve/pii/S0013794410001128>
- [40] L. Malcher, F. Andrade Pires, J. C. A. S. de A. A., *An extended GTN model for ductile fracture under high and low stress triaxiality*, International Journal of Plasticity 54 (2014) 193–228 (Mar. 2014). doi:[10.1016/j.ijplas.2013.08.015](https://doi.org/10.1016/j.ijplas.2013.08.015).  
 URL <http://linkinghub.elsevier.com/retrieve/pii/S0749641913001708>
- [41] W. Jiang, Y. Li, J. Su, *Modified GTN model for a broad range of stress states and application to ductile fracture*, European Journal of Mechanics - A/Solids 57 (2016) 132–148 (May 2016). doi:[10.1016/j.euromechsol.2015.12.009](https://doi.org/10.1016/j.euromechsol.2015.12.009).  
 URL <http://linkinghub.elsevier.com/retrieve/pii/S0997753815001710>
- [42] J. Lemaitre, *A Continuous Damage Mechanics Model for Ductile Fracture*, Journal of Engineering Materials and Technology 107 (1) (1985) 83–89 (Jan. 1985). doi:[10.1115/1.3225775](https://doi.org/10.1115/1.3225775).  
 URL <http://dx.doi.org/10.1115/1.3225775>
- [43] A. A. Benzerga, J. Besson, *Plastic potentials for anisotropic porous solids*, European Journal of Mechanics-A/Solids 20 (3) (2001) 397–434 (2001).
- [44] V. Tvergaard, *On localization in ductile materials containing spherical voids*, International Journal of Fracture 18 (4) (1982) 237–252 (1982).  
 URL <http://link.springer.com/article/10.1007/BF00015686>
- [45] Y. Zhang, E. Lorentz, J. Besson, *Ductile damage modelling with locking-free regularised gtn model*, International Journal for Numerical Methods in Engineering 113 (13) (2018) 1871–1903 (2018). arXiv:<https://onlinelibrary.wiley.com/doi/pdf/10.1002/nme.5722>, doi:[10.1002/nme.5722](https://doi.org/10.1002/nme.5722).  
 URL <https://onlinelibrary.wiley.com/doi/abs/10.1002/nme.5722>
- [46] B. Tanguy, J. Besson, *An extension of the Rousselier model to viscoplastic temperature dependent materials*, Int. J. Fracture 116 (1) (2002) 81–101 (2002).
- [47] A. Needleman, J. Rice, *Limits to ductility set by plastic flow localization*, in: e. D.P. Koistinen (Ed.), *Mechanics of Sheet Metal Forming*, Plenum Publishing Corporation, 1978, pp. 237–267 (1978).
- [48] B. Tanguy, J. Besson, R. Piques, A. Pineau, *Ductile—brittle transition of a A508 steel characterized by the Charpy impact test. Part—II: modelling of the Charpy transition curve*, Eng. Fract. Mech. 72 (2005) 413–434 (2005).
- [49] B. Tanguy, T. Luu, G. Perrin, A. Pineau, J. Besson, *Plastic and damage behavior of a high strength X100 pipeline steel: experiments and modelling*, Int. J. of Pressure Vessels and Piping 85 (5) (2008) 322–335 (2008).
- [50] R. R. U. Queiroz, F. G. G. Cunha, B. M. Gonzalez, *Study of dynamic strain aging in dual phase steel*, Mater. Sci. Engng A 543 (2012) 84–87 (2012).
- [51] R. Foerch, J. Besson, G. Cailletaud, P. Pilvin, *Polymorphic constitutive equations in finite element codes*, Computer Methods in Applied Mechanics and Engineering 141 (3) (1997) 355 – 372 (1997). doi:[https://doi.org/10.1016/S0045-7825\(96\)01111-5](https://doi.org/10.1016/S0045-7825(96)01111-5).  
 URL <http://www.sciencedirect.com/science/article/pii/S0045782596011115>
- [52] J. Besson, R. Foerch, *Large scale object-oriented finite element code design*, Computer Methods in Applied Mechanics and Engineering 142 (1) (1997) 165 – 187 (1997). doi:[https://doi.org/10.1016/S0045-7825\(96\)01124-3](https://doi.org/10.1016/S0045-7825(96)01124-3).

- URL <http://www.sciencedirect.com/science/article/pii/S0045782596011243>
- [53] J. Besson, D. Steglich, W. Brocks, Modeling of crack growth in round bars and plane strain specimens, *International journal of solids and structures* 38 (46-47) (2001) 8259–8284 (2001).
- [54] T. J. R. Hughes, *Generalization of selective integration procedures to anisotropic and nonlinear media*, *International Journal for Numerical Methods in Engineering* 15 (9) 1413–1418. arXiv:<https://onlinelibrary.wiley.com/doi/pdf/10.1002/nme.1620150914>, doi:10.1002/nme.1620150914.  
URL <https://onlinelibrary.wiley.com/doi/abs/10.1002/nme.1620150914>
- [55] J.-D. Garaud, S. Feld-Payet, F. Bettonte, A. Tireira, Y. Le Sant, G. Le Besnerais, S. Belon, *escale : plateforme logicielle pour le dialogue essai - calcul*, in: 13e colloque national en calcul des structures, Université Paris-Saclay, Giens, Var, France, 2017 (May 2017).  
URL <https://hal.archives-ouvertes.fr/hal-01908509>
- [56] E. Team, P. Galon, Europlexus: a computer program for the finite element simulation of fluid-structure systems under transient dynamic loading. User's manual., 2016 (02 2016).
- [57] E. Diamantopoulou, W. Liu, C. Labergere, H. Badreddine, K. Saanouni, P. Hu, Micromorphic constitutive equations with damage applied to metal forming, *International Journal of Damage Mechanics* 26 (2) (2017) 314–339 (2017). doi:10.1177/1056789516684650.

## List of Figures

1	Microstructure of DP450 steel after nital etching. . . . .	4
2	Specimens used in the experimental campaign (measurement points are marked with ●). Specific dimensions used at high rates are outlined in red. . . . .	5
3	Experimental setups and measure devices for quasi-static and dynamic tensile tests. . . . .	6
4	Illustration of shadow tracking measure on NT1 specimen. . . . .	6
5	Results obtained with quasi-static tensile test on standard flat specimen ( $\dot{\epsilon} = 0.001 \text{ s}^{-1}$ ) along several directions in the plane to evaluate anisotropy. . . . .	7
6	Results obtained on FN specimen at several loading rates. . . . .	8
7	Effects of sole temperature on the material behavior. . . . .	9
8	Results obtained with quasi-static tests on notched and shear specimens. . . . .	9
9	Scanning Electron Microscope pictures of a fractured NT1 specimen. . . . .	10
10	Identification of plasticity model. . . . .	16
11	Identification of the strain rate dependence model: comparison with test results. . . . .	17
12	Damage model identification results obtained with Z-opt with a mesh size of $L_e = 0.2 \text{ mm}$ . . . . .	18
13	Identification of the self-heating part of the model on large flat specimens. . . . .	19
14	Comparison between simulation and quasi-static tensile tests - part I. . . . .	22
15	Comparison between simulation and quasi-static tensile tests - part II. . . . .	23
16	Comparison between simulation and quasi-static tensile tests - part III. . . . .	24
17	Comparison between simulation and dynamic tensile tests. . . . .	26
18	Comparison between experimental and simulated temperature fields on Large flat specimen. . . . .	27

## List of Tables

1	Nominal chemical composition (weight %) . . . . .	4
---	---	---

2	Table summarizing the number of tests per configuration realized in the experimental campaign at room temperature of 20°C. Tests also performed at 100°C are marked with a red dot ●. Those used for the plasticity constitutive model identification are marked with a yellow star ★, and those used for the damage constitutive model are marked with a blue star ★. Tests realized on standard flat specimens to study anisotropy are not included. . . .	11
3	Identified parameters for a fixed mesh size of $L_e = 0.2$ mm. . . . .	20